

# Underpotential deposition of Cu on Au(111) in sulfate-containing electrolytes: a theoretical and experimental study

Jun Zhang,<sup>1</sup> Yung-Eun Sung,<sup>2</sup> Per Arne Rikvold,<sup>1,3,4,\*,†</sup> and Andrzej Wieckowski<sup>2,†</sup>

<sup>1</sup> *Supercomputer Computations Research Institute,*

*Florida State University, Tallahassee, Florida 32306-4052*

<sup>2</sup> *Department of Chemistry and Frederick Seitz Materials Research Laboratory,*

*University of Illinois, Urbana, Illinois 61801*

<sup>3</sup> *Center for Materials Research and Technology, and Department of Physics,*

*Florida State University, Tallahassee, Florida 32306-3016*

<sup>4</sup> *Centre for the Physics of Materials and Department of Physics,*

*McGill University, Montréal, Québec, CANADA<sup>‡</sup>*

(May 8, 2019)

## Abstract

We study the underpotential deposition of Cu on single-crystal Au(111) electrodes in sulfate-containing electrolytes by a combination of computational statistical-mechanics based lattice-gas modeling and experiments. The experimental methods are *in situ* cyclic voltammetry and coulometry and *ex situ* Auger electron spectroscopy and low-energy electron diffraction. The experimentally obtained voltammetric current and charge densities and adsorbate coverages are compared with the predictions of a two-component lattice-gas model for the coadsorption of Cu and sulfate. This model includes effective, lateral interactions out to fourth-nearest neighbors. Using group-theoretical ground-state calculations and Monte Carlo simulations, we estimate effective electrovalences and lateral adsorbate–adsorbate interactions so as to obtain overall agreement with experiments, including both our own and those of

other groups. In agreement with earlier work, we find a mixed  $(\sqrt{3}\times\sqrt{3})$  phase consisting of 2/3 monolayer Cu and 1/3 monolayer sulfate at intermediate electrode potentials, delimited by phase transitions at both higher and lower potentials. Our approach provides estimates of the effective electrovalences and lateral interaction energies, which cannot yet be calculated by first-principles methods.

1995 PACS Numbers: 68.45.-v 82.20.Wt 82.45.+z 81.15.Pq

## I. INTRODUCTION

Underpotential deposition (UPD) is the process by which a submonolayer or monolayer of one metal is electrochemically adsorbed onto another at electrode potentials that are positive with respect to the potential for bulk deposition. It occurs when the adsorbate adatoms are more strongly bound to the foreign substrate than to a substrate of their own kind [1]. This phenomenon has been known since the early years of this century [2–5], but its study has intensified only during the last two decades [1,6]. Current-potential data for UPD on single-crystal surfaces, obtained from cyclic voltammetry (CV) experiments, frequently display sharp current peaks [7,8]. The shapes, positions, and number of these peaks depend on the substrate and the crystal plane on which the adsorption takes place [7–9], as well as on the nature of the electrolyte [10]. It was already suggested in Refs. [7,8,11] that the CV current peaks separate ordered and disordered adsorbate structures, and it was later pointed out that the peaks themselves should correspond to phase transitions in the adsorbed layer [1,12,13]. The UPD phenomenon is of fundamental interest as an aspect of the detailed, microscopic structure of electrode–electrolyte interfaces, which is presently the focus of vigorous research [14]. It provides a means of controlling the microscopic surface structure through the electrolyte composition and the applied potential, and likely applications are suggested by the observations that metallic submonolayers have the ability to significantly modify the catalytic activity of a substrate [15], and that UPD is the first step in the liquid-phase epitaxial growth of metallic heterostructures [16].

The phase-transition aspects of UPD make this area of surface electrochemistry well suited for statistical-mechanical modeling [17–20]. The first detailed, statistical-mechanical lattice-gas model for a UPD system was introduced by Huckaby and Blum (HB), who considered the electrosorption of copper (Cu) onto the (111) plane of gold [Au(111)] in the presence of sulfate [12,13,21–26]. This system also has been intensively studied by a number of experimental techniques (see Sec. II), and the detailed data that are now available render it an excellent candidate for theoretical modeling.

In this article we present a study of the UPD of Cu on well-characterized, single-crystal Au(111) electrodes in sulfate-containing electrolytes, in which we employ both experimental and theoretical methods. The experimental techniques used are *in situ* CV and coulometry to detect the current peaks and measure the total charge transferred during the adsorption/desorption processes, and *ex situ* Auger electron spectroscopy (AES) and low-energy electron diffraction (LEED) to determine the adsorbed Cu and sulfate coverages and the adlayer structure, respectively. In the theoretical part of the study we formulate a full, two-component lattice-gas model with effective, lateral interactions out to fourth-nearest neighbors. This is a generalization of the HB model [12,13,21–26]. Using group-theoretical ground-state calculations at zero temperature [27–29] and Monte Carlo (MC) simulations at room temperature [30–32], we estimate the model parameters (the effective, lateral interactions and electrovalences) so as to obtain overall agreement with the available experimental data, including both our own and those of other groups. This theoretical approach has previously been applied to electrochemical problems by Rikvold and co-workers [33–37], and it was most recently used to model the coadsorption of hydrogen with urea on single-crystal platinum (100) electrodes [19,38–43] and with sulfate on rhodium (111) [19]. It differs from the approach taken by HB in that we apply the full, two-component lattice-gas model to analyse *global*, as well as local features of the system’s phase diagram and CV current profiles, and in that our room-temperature results are obtained by nonperturbative, numerical simulation. (For reviews and discussion of the HB approach, see Refs. [25,26].) Some preliminary results of this study have been reported in Refs. [20,44].

The remainder of this paper is organized as follows. In Sec. II we give a survey of experimental results that are currently available. In Sec. III we describe our experimental procedures and results. In Sec. IV we introduce our lattice-gas model and give the relations between the lattice-gas parameters and the experimentally observable quantities. Here we also discuss our procedure for adjusting the model parameters to fit the experiments. In Sec. V we present together our numerical and experimental results, and in Sec. VI we give a finite-size scaling analysis of the phase transitions predicted by our model. In Sec. VII we

briefly summarize our conclusions and discuss their significance.

## II. SURVEY OF THE EXPERIMENTAL SITUATION

The UPD of Cu on Au(111) in sulfate-containing electrolytes has been extensively studied, both by *in situ* techniques like CV [7,8,10,11,45–51], chronocoulometry [45–51], scanning tunneling microscopy (STM) [9,45,52,53], atomic-force microscopy (AFM) [54], Fourier-transform infrared spectroscopy (FTIR) [55], X-ray-absorption spectroscopy (EXAFS and XANES) [56–58], surface X-ray scattering [59,60], quartz crystal microbalance (QCM) [47,59], and by *ex situ* techniques, such as LEED, RHEED (reflection high-energy electron diffraction) and AES [10,11,61–63]. Electrolyte compositions used in several CV experiments (including the present work) are listed in Table I, together with potential scan rates and observed current-peak separations. The observation that the different electrolyte compositions included in Table I do not qualitatively change the shape of the voltammogram indicates that within this range of compositions the adsorbates remain the same. In this paper we assume these to be  $\text{Cu}^{2+}$  and  $\text{SO}_4^{2-}$  in solution, which are adsorbed as near-neutral Cu and partially discharged or neutralized  $\text{SO}_4^{2-}$ , respectively [48–51,64].

A three-step experiment was performed by Shi and Lipkowski [48,49] to clarify the roles of the different adsorbates. With 0.1 M perchloric acid ( $\text{HClO}_4$ ) as the only electrolyte (*i.e.*, with no copper added), the CV current in the double-layer range was weak, indicating that the ions present in the solution did not adsorb significantly on the surface. In the next step,  $\text{K}_2\text{SO}_4$  was added, introducing  $\text{HSO}_4^-$  and  $\text{SO}_4^{2-}$  ions into the solution. An adsorption peak then appeared, particularly during the positive-going scan. Radiochemical studies [64] indicate that this peak is due to sulfate adsorption with a maximum coverage of approximately 0.2 monolayers (ML). This result agrees with chronocoulometric results [64] and with earlier STM studies [65,66], in which a  $(\sqrt{3} \times \sqrt{7})$  sulfate adlayer was indicated on the positive side of the voltammetric peak in the absence of copper, without [65] or with [66] a perchloric-acid supporting electrolyte. (In UHV studies with samples emersed

at potentials for which the  $(\sqrt{3}\times\sqrt{7})$  structure is observed *in situ*, only a  $(\sqrt{3}\times\sqrt{3})$  surface structure is observed, presumably produced by desorption of water that was coadsorbed with the sulfate [67].) Finally, addition of  $\text{Cu}^{2+}$  [as  $\text{Cu}(\text{ClO}_4)_2$ ] caused the appearance of two sharp (10–30 mV wide) current peaks that totally dominate the voltammogram, as illustrated by our own data in Fig. 1(a). There is no two-peak feature in the CV if no copper is added. On the other hand, if the copper concentration is kept fixed while the concentration of sulfate is reduced, either the peak heights are reduced, or the two peaks merge, or both effects are observed together [48,49]. Evidently, the coadsorption of Cu and sulfate is mutually enhancing. (The same effects, albeit with a smaller peak separation, are also seen with Pt(111) electrodes in the same electrolytes [68].)

In Fig. 1(b) is shown the charge density transferred during the adsorption/desorption process, obtained as the integral of the CV current density in Fig. 1(a) between +120 and +420 mV *vs.* Ag/AgCl. The charge plateau in the potential region between the CV peaks (approximately 200–300 mV) lies about  $200\text{ }\mu\text{C}/\text{cm}^2$  below the charge density at 420 mV. If the reactions  $\text{Cu} - 2\text{e}^- \rightarrow \text{Cu}^{2+}$  and  $\text{SO}_4 + 2\text{e}^- \rightarrow \text{SO}_4^{2-}$  are assumed across the right-hand peak (Peak #1), the desorption of 2/3 ML of Cu and 1/3 ML of sulfate would result in a total charge transfer in that potential region of  $160\text{ }\mu\text{C}/\text{cm}^2$  [46]. This coverage–charge correspondence is supported by RHEED and LEED [11,61], by which a  $(\sqrt{3}\times\sqrt{3})$  superstructure was observed in the potential region between the peaks. Further, consistent results have been obtained by STM [9,45,52,53]. Corroborating evidence was also obtained in an *in situ* electrochemical QCM study [47]. At the left-hand peak (Peak #2) and for still more negative potentials, the Cu coverage approaches 1 ML, and EXAFS results have suggested that sulfate adsorbs on top of the Cu atoms when a monolayer of Cu has been deposited on the Au(111) surface [56]. This interpretation is supported by the measurements of Shi and Lipkowski [49] and by our own AES results. The total change can therefore not be explained by the specified charge-transfer reactions, which would predict a much larger charge transfer than the one measured. Shi and Lipkowski [48,49] derived an equilibrium

electrocapillary equation and determined the relative interfacial tension from measurements of the electrode charge density, using the back-integration technique. The Cu coverage is then simply obtained as the derivative of the relative interfacial tension with respect to the electrochemical potential of Cu. They compared the corresponding charge with the calculated Cu coverage and concluded that the effective electrovalence of copper varies from 1.6 to 1.8 in the double-peak range of the electrode potential. These results are consistent with those obtained in our present work.

The total charge transfer measured from CV results varies among the reported experiments. In the potential range from 120 to 420 mV *vs.* Ag/AgCl, which includes both CV peaks, some of the available coulometric results give values about  $-350 \mu\text{C}/\text{cm}^2$  [46,48–51] (also the result of the present work),  $-460 \mu\text{C}/\text{cm}^2$  [45], and  $-470 \mu\text{C}/\text{cm}^2$  [47], compared with the theoretical value of  $-444 \mu\text{C}/\text{cm}^2$  for a monolayer of ions transferring two electrons per ion to the Au(111) surface. According to Refs. [48,49], variation of the sulfate concentration from 0.01 mM to 5 mM changes the total charge transfer only by about 5% at the negative end of the UPD potential range. Likewise, variation of the  $\text{Cu}(\text{ClO}_4)_2$  concentration from 0.01 mM to 5 mM also did not yield significant changes in the total charge. Thus, it is highly unlikely that the large discrepancies between the experimentally measured charge transfers are due to the differences between the electrolyte compositions used. Rather, we believe that the large charge transfers observed in Refs. [45,47] were due to unexpectedly large roughness of the electrodes.

The only systematic studies of kinetic aspects of the UPD in this system of which we are aware, are by Hölzle, *et al.* [53,69,70]. They considered the dependence on the potential scan rate of the the separation between the positions of the positive- and negative-going CV current peaks (*i.e.*, the hysteresis) and the corresponding maximum current densities. In both cases they found a linear dependence on the square root of the scan rate. Additional potential-step measurements, in which the potential was changed discontinuously from one side of a peak to the other, gave indications of first-order phase transitions and phase change via a heterogeneous nucleation mechanism.

### III. EXPERIMENTAL PROCEDURES AND RESULTS

In this section we detail the experimental procedures employed in the present study, and we present our experimental results. In later sections these will be used to formulate our lattice-gas model and determine its parameters.

The combined ultra-high vacuum (UHV) and electrochemistry instrument has been described elsewhere [67,71,72]. Prior to the electrochemical experiments, the (111) plane of the gold single crystal (Johnson Matthey, 99.995% purity) was cleaned by 340 eV  $\text{Ar}^+$  ion sputtering and annealed at around 650 K. The meniscus position of the working electrode ensured that only the chosen plane of the gold crystal was exposed to the electrolyte. Following removal of the electrode from solution, a drop of electrolyte remained hanging from the surface. The drop was removed using Teflon tubing terminated with a syringe [72]. The electrode was next transferred to UHV for characterization by electron spectroscopies. There was no carbon contamination on the emersed surfaces, and gold surfaces showed complete water desorption [73].

The electrochemical measurements were conducted using conventional three-electrode circuitry and an EG&G PAR 362 potentiostat. The working solutions were made of Millipore water (18  $\text{M}\Omega\cdot\text{cm}$ ), ultra-pure grade  $\text{H}_2\text{SO}_4$  (Ultrex from VWR), and ultra-pure grade  $\text{HClO}_4$  (VWR). Solutions were deaerated and blanketed with nitrogen (Linde, Oxygen Free, 99.99%). The  $\text{CuSO}_4$  (99.999%, Aldrich) and  $\text{Na}_2\text{SO}_4$  (ACS grade, Fisher Scientific) chemicals were used as received. Voltammetric current profiles obtained at a scan rate of 2 mV/s are shown in Fig. 1. The separations between the positive- and negative-going CV peak potentials were 24 mV for Peak #1 and 44 mV for Peak #2, indicating that kinetic effects [53,69,70] may contribute to the shape of the voltammogram to a nonnegligible degree, even at this relatively low scan rate.

The AES was carried out in differentiated mode with 2 eV modulation amplitude, using a Perkin Elmer PHI-10-155 cylindrical mirror analyzer (CMA). The spectra were obtained using a digital data acquisition system, and smoothed one time using a simple 11-point



averaging technique. The analysis was performed within 5–8 seconds at a given point on the sample, after which the location on the sample was changed for a subsequent 5–8 seconds’ measurement (to reduce the electron-beam damage). These AES spectra are shown in Fig. 2.

Quantitative AES analyses of sulfate were performed using a standardization technique developed by Wieckowski and co-workers [67,71,72]. In this procedure, a thick deposit of sodium sulfate was formed after water evaporation from gold emerged from aqueous 2 M  $\text{Na}_2\text{SO}_4$ . The Au(111) surface covered by  $\text{Na}_2\text{SO}_4$  was transferred into UHV and used as a standard for the AES characterization of the electrode covered by sulfate up to 1 ML coverage. The thick, bulk-like layer of Cu deposited from a solution containing 2 M  $\text{Cu}^{2+}$  and 1 mM  $\text{H}_2\text{SO}_4$  at a negative potential served as the reference standard for the Cu intensity. We used a sensitivity factor approach within a homogenous model of the adsorbed layer, resulting from nonlinear equations discussed in Ref. [67]. The resulting coverages of sulfate [obtained from the S(LMM) Auger electron transitions] and Cu [from the Cu(LMM) and Cu(MNN) transitions] are shown *vs.* the electrode potential, together with our simulated coverage results, in Fig. 7.

Our measurements were conducted in a very diluted sulfuric acid solution (0.1 mM), containing 1 mM of copper sulfate. The low bulk concentration of copper cations ensures that practically none of the Cu-species remains in the emerged film, that could be added to the adsorbate coverage measured by AES in UHV. Therefore, no rinsing of the electrode surface before emersion to vacuum was necessary. The spot width of the hexagonal (111) LEED pattern of the surface indicates a  $(1 \times 23)$  reconstruction of the Au(111) surface, which is confirmed by the sharp CV spike in pure  $\text{H}_2\text{SO}_4$  solution, seen in Fig. 1(a) at approximately 440 mV *vs.* Ag/AgCl [67,74]. A representative LEED pattern is shown in Fig. 3.

All measurements were conducted at room temperature. Unless otherwise indicated, the electrode potentials are referred to Ag/AgCl.

#### IV. MODEL AND THEORETICAL METHODS

Our lattice-gas model for the UPD of Cu on Au(111) in sulfate-containing electrolyte is a refinement of the HB model [12,13,21–26]. It is based on the assumption that the sulfate coordinates the triangular Au(111) surface (STM indicates that the  $(1 \times 23)$  reconstruction observed by LEED (see Sec. III) does not occur *in situ* [9]) through three of its oxygen atoms, with the fourth S-O bond pointing away from the surface [12,21,23,24,60,66] (as is also the most likely adsorption geometry on Rh(111) [19]). This adsorption geometry gives the sulfate a “footprint” in the shape of an equilateral triangle with a O-O distance of 2.4 Å [75], reasonably matching the lattice constant for the triangular Au(111) unit cell, 2.88 Å [76]. The Cu is assumed to compete for the same adsorption sites as the sulfate. The configuration energies of the coadsorbed particles are given by the standard three-state lattice-gas Hamiltonian (energy function) used, *e.g.*, in Refs. [33–37]:

$$\begin{aligned} \mathcal{H}_{\text{LG}} = \sum_l \bigg[ & -\Phi_{\text{SS}}^{(l)} \sum_{\langle ij \rangle} n_i^{\text{S}} n_j^{\text{S}} - \Phi_{\text{SC}}^{(l)} \sum_{\langle ij \rangle} (n_i^{\text{S}} n_j^{\text{C}} + n_i^{\text{C}} n_j^{\text{S}}) - \Phi_{\text{CC}}^{(l)} \sum_{\langle ij \rangle} n_i^{\text{C}} n_j^{\text{C}} \bigg] \\ & - \Phi_{\text{SS}}^{(t)} \sum_{\Delta} n_i n_j n_k - \bar{\mu}_{\text{S}} \sum_i n_i^{\text{S}} - \bar{\mu}_{\text{C}} \sum_i n_i^{\text{C}} . \end{aligned} \quad (1)$$

Here  $n_i^{\text{X}} \in \{0,1\}$  is the local occupation variable for species X [X=S (sulfate) or C (copper)], and the third adsorption state (“empty” or “solvated”) corresponds to  $n_i^{\text{S}}=n_i^{\text{C}}=0$ . The sums  $\sum_{\langle ij \rangle}^{(l)}$  and  $\sum_i$  run over all  $l$ th-neighbor bonds and over all adsorption sites, respectively,  $\Phi_{\text{XY}}^{(l)}$  denotes the effective XY pair interaction corresponding to an  $l$ th-neighbor bond, and  $\sum_l$  runs over the interaction ranges. The term  $-\Phi_{\text{SS}}^{(t)} \sum_{\Delta} n_i n_j n_k$  expresses three-particle interactions between sulfates, involving all second-neighbor equilateral triangles [77–79]. Those bonds that correspond to potentially nonzero lateral interactions in the present implementation of our model are shown in Fig. 4. For large separations the interactions are assumed to vanish, and  $\Phi_{\text{SS}}^{(1)}$  is an infinite repulsion corresponding to nearest-neighbor sulfate-sulfate exclusion (“hard hexagons” [21,23,24,80]). The change in electrochemical potential when one X particle is removed from the bulk solution and adsorbed on the surface is  $-\bar{\mu}_{\text{X}}$ . The sign convention is such that  $\Phi_{\text{XY}}^{(l)} > 0$  denotes an effective attraction, and  $\bar{\mu}_{\text{X}} > 0$  denotes a

tendency for adsorption in the absence of lateral interactions. We emphasize that the  $\Phi_{XY}^{(l)}$  are *effective* interactions through several channels, including electron-, phonon-, electrostatic, and fluid-mediated mechanisms (see Refs. [20,36] for discussion and references).

The electrochemical potentials in Eq. (1) are (in the weak-solution approximation and here given in molar units) related to the bulk concentrations  $[X]$  and the electrode potential  $E$  as

$$\begin{aligned}\bar{\mu}_S &= \mu_S^0 + RT \ln \frac{[S]}{[S]^0} - z_S F E \\ \bar{\mu}_C &= \mu_C^0 + RT \ln \frac{[C]}{[C]^0} - z_C F E.\end{aligned}\tag{2}$$

Here  $z_S$  and  $z_C$  are the effective electrovalences of sulfate and copper, respectively,  $R$  is the molar gas constant,  $T$  is the absolute temperature, and  $F$  is the Faraday constant. The quantities superscripted with a 0 are reference values which contain the local binding energies to the surface. They are generally temperature dependent due, among other effects, to rotational and vibrational modes.

The coverages of sulfate and Cu,  $\Theta_S$  and  $\Theta_C$ , are the thermodynamic densities conjugate to  $\bar{\mu}_S$  and  $\bar{\mu}_C$ , respectively. They are defined as

$$\Theta_X = N^{-1} \sum n_i^X,\tag{3}$$

where  $N$  is the total number of unit cells in the surface lattice. However, it is experimentally observed that the sulfate species remains partially adsorbed on top of the complete monolayer of Cu in the negative-potential region, rather than becoming desorbed into the solution [49,56], as was mentioned in Sec. II. Rather than introducing a full, two-layer lattice-gas model, we approximate the sulfate coverage in this second layer as

$$\Theta_S^{(2)} = \alpha \Theta_C (1/3 - \Theta_S),\tag{4}$$

which allows the difference between the first-layer coverage  $\Theta_S$  and its saturation value of  $1/3$  to be transferred to the top of the Cu layer. The factor  $\alpha$  is a phenomenological fitting parameter expected to be between zero and one. The total sulfate coverage measured, *e.g.*, in

chronocoulometric [49] and AES experiments, is  $\Theta_S + \Theta_S^{(2)}$ , and the total charge transported across the surface per unit cell during the adsorption/desorption process thus becomes

$$\begin{aligned} q &= -e \left[ z_C \Theta_C + z_S (\Theta_S + \Theta_S^{(2)}) \right] \\ &= -e [(z_C + \alpha z_S/3) \Theta_C - z_S \alpha \Theta_C \Theta_S + z_S \Theta_S], \end{aligned} \quad (5)$$

where  $e$  is the elementary charge unit. In the absence of diffusion and double-layer effects and in the limit that the potential scan rate  $dE/dt \rightarrow 0$  [81], the voltametric current  $i$  per unit cell of the surface is the time derivative of  $q$ . Using differentiation by parts involving the relations between the electrode potential and the electrochemical potentials, Eq. (2), as well as the Maxwell relation  $\partial \Theta_S / \partial \bar{\mu}_C = \partial \Theta_C / \partial \bar{\mu}_S$ , we find the current density  $i$  in terms of the lattice-gas response functions  $\partial \Theta_X / \partial \bar{\mu}_Y$ :

$$\begin{aligned} i &= eF \left\{ z_S^2 (1 - \alpha \Theta_C) \frac{\partial \Theta_S}{\partial \bar{\mu}_S} \Big|_{\bar{\mu}_C} + z_C (z_C - 2\alpha z_S \Theta_S/3) \frac{\partial \Theta_C}{\partial \bar{\mu}_C} \Big|_{\bar{\mu}_S} \right. \\ &\quad \left. + z_S (2z_C + \alpha z_S (1/3 - \Theta_S) - \alpha z_C \Theta_C) \frac{\partial \Theta_S}{\partial \bar{\mu}_C} \Big|_{\bar{\mu}_S} \right\} \frac{dE}{dt}, \end{aligned} \quad (6)$$

which reduces to its standard form for  $\alpha = 0$  [19,39–41]. We emphasize that the derivation of Eq. (6) is based on *equilibrium* statistical mechanics. Very close to a phase transition it may require exceedingly slow scan rates to be valid, due to critical slowing-down in the case of second-order transitions [30–32] or hysteresis in the case of first-order transitions [53,69,70,82].

The following steps are involved in adjusting the lattice-gas parameters to fit the experimental data.

**A.** Ground-state calculations [27–29] to determine parameter ranges that yield ground states which correspond to the experimentally observed phases at room temperature [25].

**B.** MC simulations [30–32] at room temperature to further adjust the effective interactions to obtain reasonable agreement with the shapes of the observed adsorption isotherms and CV profiles.

**C.** With the effective interactions obtained in step **B**, determination of the effective electrovalences so as to give agreement between the dependences of the CV peak positions on

the electrolyte composition in experiments and simulations.

**D.** Iteration of steps **B** and **C** as necessary to improve the agreement between the experiments and simulations.

### A. Ground-State Calculations

Ordered phases with unit cells up to  $(3 \times 3)$  were identified by applying the group-theoretical arguments of Landau and Lifshitz [27–29]. The ground-state energy of each phase depends on  $\bar{\mu}_S$  and  $\bar{\mu}_C$  and the lateral interactions. Among phases with identical coverages of Cu and sulfate, those were excluded that have a higher ground-state energy than others with the same coverages for all chemically reasonable choices of interaction energies. Out of the 44 remaining phases, ten were found to be realized as ground states for interactions in the range of experimental interest. These are listed in Table II, where they are identified by the notation  $(X \times Y)_{\Theta_C}^{\Theta_S}$ . For a given set of interactions, the zero-temperature phase boundaries were exactly determined by pairwise equating the energies given in Table II. In order to easily explore the effects of changing one or more of the interactions, a computer program was developed which numerically determines the ground-state diagram by scanning  $\bar{\mu}_S$  and  $\bar{\mu}_C$  and determining the phase of minimum ground-state energy [83].

The ground-state diagram obtained with the final set of interaction constants used in this work is shown in Fig. 5. For large negative  $\bar{\mu}_S$  only Cu adsorption is possible, and the phase diagram is that of the lattice-gas model corresponding to the triangular-lattice antiferromagnet with next-nearest neighbor ferromagnetic interactions [84–86]. Similarly, in the limit of large positive  $\bar{\mu}_S$  and large negative  $\bar{\mu}_C$  the zero-temperature phase is the  $(\sqrt{3} \times \sqrt{3})_0^{1/3}$  sulfate phase characteristic of the hard-hexagon model [12,21,23,24,80]. The phase diagram for intermediate electrochemical potentials is quite complicated. For  $\bar{\mu}_S < -22$  kJ/mol, no sulfate adsorption occurs in the first adlayer, while for  $\bar{\mu}_C < -18$  kJ/mol, no Cu is adsorbed. The  $(\sqrt{3} \times \sqrt{3})_{2/3}^{1/3}$  mixed-phase region in the upper right-hand part of the diagram is relatively large, due to the nearest-neighbor effective attraction between Cu and

sulfate,  $\Phi_{\text{SC}}^{(1)}$ . This is the mixed phase which occurs between the CV peaks. The  $(\sqrt{3}\times\sqrt{7})_0^{1/5}$  phase corresponds to experimental observations in copper-free systems [52,66]. This phase is enhanced by the fourth-neighbor sulfate-sulfate attraction,  $\Phi_{\text{SS}}^{(4)}$ , and the  $(\sqrt{3}\times\sqrt{3})_0^{1/3}$  (“hard-hexagon”) phase (which has not been directly observed in this system) is disfavored by  $\Phi_{\text{SS}}^{(t)}$ , the second-neighbor repulsive trio interactions. The  $(\sqrt{3}\times\sqrt{7})_0^{1/5}$  phase is also very sensitive to the next-nearest neighbor interaction  $\Phi_{\text{SS}}^{(2)}$ . Attractive values of this interaction favor the  $(\sqrt{3}\times\sqrt{3})_0^{1/3}$  phase, whereas repulsive values favor the  $(\sqrt{7}\times\sqrt{7})_0^{1/7}$  phase. The experimental observations of the  $(\sqrt{3}\times\sqrt{7})_0^{1/5}$  phase therefore indicate that  $\Phi_{\text{SS}}^{(2)}$  must be much weaker than the other effective interactions, and we set it equal to zero in our simulations.

## B. Simulations at Room Temperature

At nonzero temperatures, the thermodynamic and structural properties of a lattice-gas model can be obtained by a number of analytical and numerical methods. These include mean-field approximations [87,88], Padé-approximant methods based on liquid theory [12,13,17,21–24], numerical transfer-matrix calculations [33–38], and MC simulations [19,20,35,39–44]. The reason for our choice of the numerical MC method [30–32] is that such non-perturbative methods as MC and transfer-matrix calculations provide much more accurate results for two-dimensional systems than even quite sophisticated mean-field approximations [89]. Yet they are quite easy to program, and with modern computer technology their implementation is well within even modest computational resources. (All our numerical data were produced on a cluster of IBM RS/6000 workstations.) For models with such relatively long-ranged interactions as the present one, MC is better suited than numerical transfer-matrix methods.

The ground-state diagram serves as a guide to the path in the  $(\bar{\mu}_S, \bar{\mu}_C)$  plane that the room-temperature isotherms should follow. At constant temperature and  $p\text{H}$ , two factors influence the path: the adsorbate concentrations in the bulk, and the effective electrovalences. As seen from Eq. (2),  $\bar{\mu}_S$  and  $\bar{\mu}_C$  depend linearly on  $E$ , with proportionality constants  $-z_S$

and  $-z_C$ , which must be determined from experiments. In order to obtain the parts of the room-temperature phase diagram of the model that are relevant to the experiments, we performed initial isothermal potential scans, using the approximate values  $z_S = -2$  and  $z_C = +2$ , which correspond to the full ionic charges of  $\text{SO}_4^{2-}$  and  $\text{Cu}^{2+}$ , respectively. The experimental evidence, in particular Refs. [48,49,51], indicates that these ‘ideal’ values are somewhat too large. After obtaining the room-temperature phase boundaries as discussed in this Subsection, we therefore re-adjusted our estimates of  $z_S$  and  $z_C$  as discussed in Subsec. IV C below.

The MC simulations used to obtain adsorption isotherms and CV currents at room temperature ( $RT = 2.50\text{kJ/mol}$ , corresponding to  $28^\circ\text{C}$ ) were performed on triangular lattices of size  $L \times L$ , using a heat-bath algorithm [30–32] with updates at randomly chosen sites. The majority of our simulations were performed with  $L=30$ , supplemented with simulations for  $L=45$  and  $15$ . Simulation results reported without specifying the system size are for  $L=30$ .

In order to avoid getting stuck in metastable configurations (a problem which is exacerbated by the nearest-neighbor sulfate-sulfate exclusion), we simultaneously updated clusters consisting of two nearest-neighbor sites. Each data point was obtained from a run of  $10^5$  Monte Carlo steps per site (MCSS), starting from the appropriate ground-state configuration. Sampling was performed at intervals of 50 MCSS, and the first 4000 MCSS were discarded to ensure equilibration. The coverages were obtained as averages over these samples, and the nonordering lattice-gas response functions,  $\partial\Theta_S/\partial\bar{\mu}_S$ ,  $\partial\Theta_C/\partial\bar{\mu}_C$ , and  $\partial\Theta_S/\partial\bar{\mu}_C = \partial\Theta_C/\partial\bar{\mu}_S$ , and the adsorbate heat capacity were calculated from the equilibrium coverage and energy fluctuations in the standard way [30–32].

The lattice-gas interaction energies were varied until the widths of the CV peaks corresponding to the room-temperature phase boundaries were in acceptable agreement with the experimentally observed peak widths. The corresponding peak positions are superimposed on the ground-state diagram in Fig. 5.

### C. Effective Electrovalences

Once the room-temperature phase boundaries for the chosen set of interaction constants had been calculated, the effective electrovalences could be re-estimated by comparing the simulated phase boundaries (CV peak positions) in the  $(\bar{\mu}_S, \bar{\mu}_C)$  plane with the dependence on the electrolyte composition of experimentally observed CV peak potentials. For this purpose we used data from Omar *et al.* [46], who measured the CV peak positions *vs.* the bulk concentration of  $\text{Cu}^{2+}$  ions at almost constant bulk sulfate concentration, as summarized in Table III.

A theoretical phase boundary can be represented by a functional relationship,  $\bar{\mu}_S^{\text{peak}} = f(\bar{\mu}_C^{\text{peak}})$ . Combining this with Eq. (2) and differentiating with respect to  $\ln[C]$ , we obtain

$$z_C - (f'_i)^{-1} z_S = \frac{RT}{F} \left( \frac{dE_i^{\text{peak}}}{d \ln[C]} \right)^{-1}, \quad (7)$$

where  $f'$  is the derivative of  $f$  with respect to its argument, and the subscripts identify the particular peak in question. In the parameter region of interest, both the theoretical phase boundary and the experimental dependence of the peak potentials on  $\ln[C]$  are reasonably approximated by straight lines. Therefore, combining the results for both CV peaks, one obtains two linear equations for the two unknown quantities,  $z_C$  and  $z_S$ . Using our simulated data,  $(f'_1)^{-1} = -0.52 \pm 0.03$  and  $(f'_2)^{-1} = +0.66 \pm 0.07$ , together with the experimentally obtained  $(dE_1^{\text{peak}}/d \ln[C])^{-1} = +42 \pm 3 \text{ V}^{-1}$  and  $(dE_2^{\text{peak}}/d \ln[C])^{-1} = +94 \pm 6 \text{ V}^{-1}$ , we obtain  $z_C = +1.68 \pm 0.09$  and  $z_S = -1.14 \pm 0.16$ , where the uncertainties only include statistical errors. (If, instead, we had used the theoretical ground-state values,  $(f'_1)^{-1} = -0.5$  and  $(f'_2)^{-1} = +1.0$ , obtained by equating the ground-state energies in Table. II, we would have obtained  $z_C = +1.54 \pm 0.07$  and  $z_S = -0.90 \pm 0.12$ .)

These values of  $z_C$  and  $z_S$  should be considered as averages of weakly potential- and concentration-dependent electrovalences in the region of experimental interest. To within the error bars they agree with the values recently obtained by Shi *et al.* [49,51] by electrocapillary techniques.



#### D. Further Parameter Refinement

In principle, Steps **B** and **C** above can be iterated to further improve the agreement between theory and experiment and correspondingly obtain improved parameter estimates. However, as shown in the following sections our simulated and experimentally measured data agree to a quite satisfactory degree, using the lattice-gas parameters obtained after one iteration. Since the iteration process is expensive, both in terms of human and computer time, we therefore terminated the loop after the first pass through Step **C**. Our final MC simulations were performed with the effective interactions listed in Fig. 4, using  $z_C=+1.70$  and  $z_S=-1.15$ .

#### V. COMPARISON OF SIMULATED AND EXPERIMENTAL RESULTS

The room-temperature potential-scan path corresponding to the electrolyte composition used in our experiments, was chosen such that the theoretical CV peak separation along the scan equals the peak separation in the experimental data shown in Figs. 1(b) and 6(a). This scan is indicated by the dotted line labeled “1” in Fig. 5. The simulated CV current density [Eq. (6)] along this potential scan is shown together with our experimentally measured current (positive-going scan) in Fig. 6(a), and the corresponding integrated charge densities [Eq. (5)] are shown in Fig. 6(b). As we pointed out in Sec. II, there is previous experimental evidence that at the negative end of the UPD potential range, sulfate adsorbs as a submonolayer on top of the monolayer of Cu, with a coverage  $\Theta_S^{(2)} \approx 0.2$  [49]. These results agree fully with our AES results, which are shown in Fig. 7. The corresponding value of  $\alpha = 0.6$  in Eq. (5) was used to obtain the CV current and surface-charge densities shown in Fig. 6 and the sulfate coverage shown in Fig. 7 from the lattice-gas simulations.

With the aid of the ground-state diagram in Fig. 5 it is easy to analyse the simulated and experimental results shown in Figs. 6 and 7. Starting from the negative end, we scan in the direction of positive electrode potential (*i.e.*, from upper left to lower right in Fig. 5).

Near the CV peak at approximately 200 mV (Peak #2), sulfate begins to compete with Cu for the gold surface sites, resulting in a third of the Cu desorbing and being replaced by sulfate over a potential range of about 30 mV. Due to the strong effective attraction between the sulfate and Cu adparticles,  $\Phi_{\text{SC}}^{(1)}$ , a mixed  $(\sqrt{3} \times \sqrt{3})_{2/3}^{1/3}$  phase is formed, which extends through the entire potential region between the two CV peaks. The  $(\sqrt{3} \times \sqrt{7})_{4/5}^{1/5}$  phase which occurs in a narrow band in the ground-state diagram between this phase and the  $(1 \times 1)_1^0$  phase that corresponds to the full Cu monolayer, is not sufficiently stable to be observed at room temperature.

As the CV peak at approximately 300 mV (Peak #1) is reached, most of the copper is desorbed within a potential range of 10 mV. As it is thus deprived of the stabilizing influence of the coadsorbed Cu, the sulfate is partly desorbed, reducing  $\Theta_{\text{S}}$  from  $1/3$  to approximately 0.05. The  $(\sqrt{3} \times \sqrt{7})_0^{1/5}$  phase in the potential region near 420 mV is consistent with experimental observations on copper-free systems [52,66]. Eventually, more positive electrode potentials cause the sulfate to form its saturated  $(\sqrt{3} \times \sqrt{3})_0^{1/3}$  hard-hexagon phase near 500 mV. Since this phase has not been experimentally observed in *in situ* experiments for this system, this is probably an artifact of the model at very positive electrode potentials.

The scenario described here corresponds closely to that proposed by HB [12,21,23,24], and the structure proposed for the mixed  $(\sqrt{3} \times \sqrt{3})_{2/3}^{1/3}$  phase between the two CV peaks has recently been strongly supported by Toney *et al.* with *in situ* surface X-ray scattering [60]. The nearly linear dependence of the two coverages on each other for  $\Theta_{\text{C}}$  between approximately 0.1 and 0.6, together with the broad maximum of the differential coadsorption ratio,  $[d(\Theta_{\text{S}} + \Theta_{\text{S}}^{(2)})/d\Theta_{\text{C}}]$  is close to 0.5 in this region] are shown in Fig. 8. (Also compare Fig. 8(a) with the insert in Fig. 4(b) of Ref. [49].) These results show that this system provides an example of the enhanced-adsorption phenomenon described by Rikvold and Deakin [36].

Very close to the phase transitions, the CV current profile may be significantly distorted from the equilibrium result represented by Eq. (6) due to kinetic effects. In addition, the transition may be rounded by defects or impurities on the adsorbent surface, which can

have significant effects even at very low concentrations [90]. As a result of these effects, the simulated quantities that are most reliably compared with experimental results are the CV currents some distance away from their maxima, and the corresponding charge densities. With this caveat, we find the agreement between our simulations and experiments quite good. The shape of the foot region of Peak #2 is well reproduced [Fig. 6(a)], and the simulated charge transfer across that peak agrees with the experimental value to within about 15% [Fig. 6(b)]. Likewise, good agreement is found with the Cu and sulfate coverages measured by AES [Fig. 7]. The background current in the ordered-phase region between the peaks also shows excellent agreement [Fig. 6(a)]. Somewhat less satisfactory agreement is obtained for Peak #1. The simulated peak is somewhat too narrow at the base, and the foot on the positive-potential side of the peak, although visible, is lower than its experimental counterpart. We find these discrepancies between the simulated and observed current densities (which were recorded at a potential scan rate of 2 mV/s and show noticeable hysteresis) to be within what one should expect from our essentially equilibrium calculation, even if the effective lattice-gas interaction were highly accurate. We therefore believe that a study of the effects of kinetics and defects in our model would be very valuable.

To investigate the effects of changing the electrolyte concentration in the lattice-gas model, two additional isothermal potential-scan paths were simulated. We assumed the same bulk sulfate concentration as for Path 1 and changed  $\bar{\mu}_C$  [Eq. (2)] to simulate bulk copper concentrations of 5 mM (Path 2) and 0.2 mM (Path 3), respectively. All three paths are shown in Fig. 5 as dotted straight lines. Simulations of current densities and coverages corresponding to Paths 2 and 3 are shown in Figs. 9(a) and 9(b), respectively. Along Path 2, which corresponds to the highest sulfate concentration, a wider potential interval is required to traverse the mixed-phase region; hence the CV peak separation is larger than for Path 1. Path 3, conversely, corresponds to the lowest sulfate concentration. It exits quickly from the  $(\sqrt{3} \times \sqrt{3})_{2/3}^{1/3}$  phase into the disordered low-coverage phase, giving a CV peak separation that is smaller than for the other two paths, as well as lower coverages of both Cu and sulfate immediately to the positive-potential side of Peak #1. We also

note that the experimentally observed asymmetric shape of the foot of Peak #1 is enhanced for lower bulk copper concentrations, as is particularly evident from the CV current along Path 3, shown in Fig. 9(a).

## VI. FINITE-SIZE SCALING ANALYSIS

The model studied here is equivalent to a generalized triangular-lattice Blume-Emery-Griffiths (BEG) [92] model with interactions of longer than nearest-neighbor range. The lattice-gas Hamiltonian in Eq. (1) can be transformed into that of the equivalent BEG model by the following transformation,

$$M = \Theta_C - \Theta_S \quad (8a)$$

$$Q = \Theta_C + \Theta_S \quad (8b)$$

$$H = \frac{1}{2} (\bar{\mu}_C - \bar{\mu}_S) \quad (8c)$$

$$D = -\frac{1}{2} (\bar{\mu}_C + \bar{\mu}_S) , \quad (8d)$$

where  $M$  is the density conjugate to  $H$ , and  $Q$  is the density conjugate to  $-D$ .

By comparing the topology of the ground-state diagram shown in Fig. 5 with those for the generalized BEG models illustrated in Refs. [34–38,93,94], one can deduce the order and universality class of the phase transitions that correspond to CV Peak #1 and #2.

The transition at Peak #1 corresponds to the phase transition seen in the BEG models as  $D$  is increased for small nonzero values of  $H$  and  $T$ . This is a first-order transition in which the total coverage  $Q$  drops discontinuously from near one to near zero. As is generally the case for first-order transitions [31], the adsorbate heat capacity  $C$  and the nonordering response functions,  $\partial M/\partial H$  and  $\partial Q/\partial D$ , diverge proportionally with the system area,  $L^2$ . This divergence is an expression of the discontinuities in  $M$  and  $Q$  (or equivalently in  $\Theta_C$  and  $\Theta_S$ ) and the latent heat associated with a first-order transition.

The transition at Peak #2 corresponds to the phase transition seen in the BEG models as  $H$  is increased for low  $T$  and negative  $D$ . This is a second-order transition which for a

system on a triangular lattice is in the same universality class as the hard-hexagon model, namely that of the three-state Potts model [27]. The standard critical exponents in this universality class are  $\nu = \frac{5}{6}$  for the correlation length,  $\alpha = \frac{1}{3}$  for the heat capacity, and  $\beta = \frac{1}{9}$  for the order parameter [95]. At a second-order phase transition the heat capacity diverges with the system size as  $L^{\alpha/\nu}$  [31], which for this universality class becomes  $L^{2/5}$ . The nonordering response functions are coupled to the heat capacity and are expected to share the same divergence [96].

We have checked these predictions by MC simulations for systems with  $L=15, 30$ , and  $45$ . The results are shown for Peak #1 *vs.*  $L^2$  in Fig. 10(a) and for Peak #2 *vs.*  $L^{2/5}$  in Fig. 10(b). (To reduce the effects of the finite-size rounding of the phase transitions, we show only the scaling results for the response functions corresponding to a direction pointing away from the transition line in the phase diagram,  $-RT(\partial Q/\partial D)$  for Peak #1 and  $RT(\partial M/\partial H)$  for Peak #2. In both cases the response function not shown has the same scaling behavior as the one shown, but its magnitude is much smaller.) The results shown in Fig. 10 are consistent with the scaling relations predicted above.

## VII. DISCUSSION AND CONCLUSIONS

In this study we have combined a computational and theoretical lattice-gas modeling approach with electrochemical and UHV experiments to study the UPD of Cu on Au(111) single-crystal electrodes in the presence of sulfate. In agreement with other experimental and theoretical studies we find that in the potential region between the two sharp CV peaks, the electrode is covered by a mixed adlayer of  $(\sqrt{3}\times\sqrt{3})R30^\circ$  symmetry, consisting of  $2/3$  ML Cu and  $1/3$  ML sulfate. This ordered-phase region is limited on the positive-potential side by a first-order phase transition to a disordered low-coverage phase, followed at still higher potentials by transitions to pure sulfate phases. On the negative-potential side the mixed phase terminates at a second-order phase transition to a full monolayer of Cu. The mixed phase is stabilized by relatively strong, effective attractive interactions between

nearest-neighbor copper and sulfate adparticles.

The lattice-gas parameters were obtained by a three-step procedure. First, a group-theoretical ground-state calculation was used to determine the intervals of interaction energies which produce ordered phases that agree with the experimental observations. Second, MC simulations were used to produce adsorbate coverages and CV current profiles at room temperature, and the interaction energies were adjusted until optimal agreement with all the available experimental data was obtained. Third, the effective electrovalences were adjusted to obtain agreement between the simulations and experiments regarding the dependences of the CV peak potentials on the bulk copper concentration. Our final estimates for the effective lateral interactions are given in Fig. 4. It is difficult to attach error estimates to these values, and there is no guarantee that even better overall agreement could not be obtained with a different parameter set. Seen as a formal optimization problem, the parameter adjustment we have performed here by the procedure detailed in Subsecs. IV A–D, is a daunting task. We are currently studying strategies that could, at least to some extent, improve the reliability of the parameter optimization procedure with a manageable computational effort [91]. However, no first-principles method exists that could calculate the effective lattice-gas parameters in this complicated, metal–water–multi-ion system with the degree of accuracy needed to calculate thermodynamic and structural quantities for quantitative comparison with experiments [97,98]. We are of the opinion that our approach represents the only method for determining effective interaction energies in complicated electrochemical systems, which is practically feasible at the present stage of theoretical and computational development.

Despite the cautionary note sounded in the preceding paragraph, we point out that our estimated interactions appear entirely sensible from a chemical point of view. Two aspects of the interactions are particularly interesting. First, the effective nearest-neighbor sulfate-Cu attraction is relatively strong:  $\Phi_{\text{SC}}^{(1)} = +4.0$  kJ/mol. This is consistent with the short Cu-O bond length (2.15 Å) found in recent *in situ* X-ray diffraction measurements [60]. Second, and perhaps more surprisingly: the nearest-neighbor Cu-Cu interaction is

moderately repulsive:  $\Phi_{\text{CC}}^{(1)} = -1.8$  kJ/mol. However, interaction energies on surfaces are usually much weaker than the interactions between the same atoms in the bulk solid, and the presence of the fluid and residual charges on the adsorbed particles may further modify the effective interactions to turn attraction into repulsion [1]. For the present system, the conclusion that nearest-neighbor Cu adparticles interact repulsively with each other, was already reached by Magnussen *et al.* [9]. We consider it a measure of the robustness of our parameter-estimation procedure that we arrived at the repulsive nature of this effective interaction independently and only after lengthy attempts at obtaining a reasonable shape for Peak #2 with an attractive nearest-neighbor interaction had failed.

The residual disagreement between our simulated and experimental results near the CV current peaks most likely arise from defects on the electrode surface, and from the use of equilibrium statistical mechanics to study in detail a phenomenon that has significant kinetic aspects. We believe that the effects of defects and kinetics in our model present promising research topics, and we hope to return to their study in the future.

## ACKNOWLEDGMENTS

Helpful comments on the manuscript were provided by M. A. Novotny, R. A. Ramos, and S. W. Sides. P. A. R. appreciates the hospitality and support of the Centre for the Physics of Materials and the Department of Physics of McGill University during the final stages of this work. This research was supported by Florida State University through the Supercomputer Computations Research Institute (DOE Contract No. DE-FC05-85-ER25000) and the Center for Materials Research and Technology, and by NSF grant No. DMR-9315969. Work at The University of Illinois was supported by NSF grant No. CHE-9411184 and by the Frederick Seitz Materials Research Laboratory under DOE Contract No. DE-AC02-76-ER01198.

## REFERENCES

\* Electronic address: rikvold@scri.fsu.edu .

† Corresponding authors.

‡ Temporary address.

- [1] D. M. Kolb, in *Adv. Electrochem. Electrochem. Eng.*, edited by H. Gerischer and W. Tobias (Wiley, New York, 1978), Vol. 11, p. 125.
- [2] G. von Hevesy, *Physik. Z.* **13**, 715 (1912).
- [3] L. B. Rogers, D. P. Krause, J. C. Griess Jr., and D. B. Ehrlinger, *J. Electrochem. Soc.* **95**, 33 (1949).
- [4] T. Mills and G. M. Willis, *J. Electrochem. Soc.* **100**, 452 (1953).
- [5] R. C. DeGeiso and L. B. Rogers, *J. Electrochem. Soc.* **106**, 433 (1959).
- [6] D. M. Kolb, *The Initial Stages of Metal Deposition: An Atomistic View*, Schering Lecture's Publications, Vol. 2, (Schering Research Foundation, Berlin, 1991).
- [7] J. W. Schultze and D. Dickertmann, *Surf. Sci.* **54**, 489 (1976).
- [8] D. Dickertmann, F. D. Koppitz, and J. W. Schultze, *Electrochim. Acta* **21**, 967 (1976).
- [9] O. M. Magnussen, J. Hotlos, G. Beitel, D. M. Kolb, and R. J. Behm, *J. Vac. Sci. Technol. B* **9**, 969 (1991).
- [10] M. Zei, G. Qiao, G. Lempfuhl, and D. M. Kolb, *Ber. Bunsen Ges. Phys. Chem.* **91**, 3494 (1987).
- [11] H. O. Beckmann, H. Gerischer, D. M. Kolb, and G. Lehmpfuhl, *Symp. Faraday. Soc.* **12**, 51 (1977).
- [12] D. A. Huckaby and L. Blum, *J. Electroanal. Chem.* **315**, 255 (1991).



- [13] L. Blum and D. A. Huckaby, J. Chem. Phys. **94**, 6887 (1991).
- [14] *Proceedings of The International Union for Vacuum Science, Theory and Applications (IUVSTA) Workshop on Surface Science and Electrochemistry*, San Benedetto del Tronto, Italy, September 12–16, 1994, edited by S. Trasatti and K. Wandelt, Surf. Sci. **335** (1995).
- [15] R. Adžić, in *Adv. Electrochem. Electrochem. Eng.*, edited by H. Gerischer (Wiley, New York, 1984), Vol. 13, p. 159, and references cited therein.
- [16] *Physics, Fabrication, and Applications of Multilayered Structures*, edited by P. Dhez and C. Weisbusch (Plenum, New York, 1988).
- [17] D. Huckaby and L. Blum, J. Chem. Phys. **92**, 2646 (1990).
- [18] L. Blum, Adv. Chem. Phys. **78**, 171 (1990).
- [19] P. A. Rikvold, M. Gamboa-Aldeco, J. Zhang, M. Han, Q. Wang, H. L. Richards, and A. Wieckowski, Surf. Sci. **335**, 389 (1995).
- [20] P. A. Rikvold, J. Zhang, Y.-E. Sung, and A. Wieckowski, *Electrochim. Acta*, in press (1996).
- [21] D. A. Huckaby and L. Blum, *Electrochem. Soc. Conf. Proc. Ser.* **92-1**, 139 (1992).
- [22] L. Blum and D. A. Huckaby, *Electrochem. Soc. Conf. Proc. Ser.* **93-5**, 232 (1993).
- [23] L. Blum and D. A. Huckaby, J. Electroanal. Chem. **375**, 69 (1994).
- [24] L. Blum, M. Legault, and P. Turq, J. Electroanal. Chem. **379**, 35 (1994).
- [25] D. A. Huckaby and L. Blum, *Langmuir*, in press.
- [26] L. Blum, D. A. Huckaby, and M. Legault, *Electrochim. Acta*, in press.
- [27] E. Domany, M. Schick, J. S. Walker, and R. B. Griffiths, Phys. Rev. B **18**, 2209 (1978).

- [28] E. Domany and M. Schick, Phys. Rev. B **20**, 3828 (1979).
- [29] M. Schick, Prog. Surf. Sci. **11**, 245 (1981).
- [30] See, *e.g.*, K. Binder, in *Monte Carlo Methods in Statistical Physics, Second Edition*, edited by K. Binder (Springer, Berlin, 1986).
- [31] K. Binder, Ann. Rev. Phys. Chem. **43**, 33 (1992).
- [32] See, *e.g.*, K. Binder and D. W. Heermann, *Monte Carlo Simulation in Statistical Physics. An Introduction. Second Edition.* (Springer, Berlin, 1992).
- [33] P. A. Rikvold, J. B. Collins, G. D. Hansen, J. D. Gunton, and E. T. Gawlinski, Mat. Res. Soc. Symp. Proc. **111**, 249 (1988).
- [34] P. A. Rikvold, J. B. Collins, G. D. Hansen, and J. D. Gunton, Surf. Sci. **203**, 500 (1988).
- [35] J. B. Collins, P. Sacramento, P. A. Rikvold, and J. D. Gunton, Surf. Sci. **221**, 277 (1989).
- [36] P. A. Rikvold and M. R. Deakin, Surf. Sci. **294**, 180 (1991).
- [37] P. A. Rikvold, Electrochim. Acta **36**, 1689 (1991).
- [38] P. A. Rikvold and A. Wieckowski, Phys. Scr. **T44**, 71 (1992).
- [39] P. A. Rikvold, A. Wieckowski, and Q. Wang, Electrochem. Soc. Conf. Proc. Ser. **93-5**, 198 (1993).
- [40] P. A. Rikvold, A. Wieckowski, Q. Wang, C. K. Rhee, and M. Gamboa, in *Computer Simulation Studies in Condensed Matter Physics VI*, edited by D. P. Landau, K. K. Mon, and H. B. Schüttler (Springer, Berlin, 1993), p. 162.
- [41] M. Gamboa-Aldeco, P. Mrozek, C. K. Rhee, A. Wieckowski, P. A. Rikvold, and Q. Wang, Surf. Sci. Lett. **297**, L135 (1993).
- [42] L. Hightower, Q. Wang, P. A. Rikvold, M. Gamboa-Aldeco, and A. Wieckowski, FSU-

- SCRI Video (1994), Electronically available in MPEG format via World Wide Web at <http://www.scri.fsu.edu/~rikvold/>.
- [43] M. Gamboa-Aldeco, C. K. Rhee, A. Nahlé, Q. Wang, J. Zhang, H. L. Richards, P. A. Rikvold, and A. Wieckowski, *Electrochem. Soc. Conf. Proc. Ser.* **94-21**, 184 (1994).
  - [44] J. Zhang, P. A. Rikvold, Y.-E. Sung, and A. Wieckowski, in *Computer Simulation Studies in Condensed Matter Physics VIII*, edited by D. P. Landau, K. K. Mon, and H. B. Schüttler (Springer, Berlin, in press).
  - [45] T. Hachiya, H. Honbo, and K. Itaya, *J. Electroanal. Chem.* **315**, 275 (1991).
  - [46] I. H. Omar, H. J. Pauling, and K. Jüttner, *J. Electrochem. Soc.* **140**, 2187 (1993).
  - [47] G. L. Borges, K. K. Kanazawa, J. G. Gordon, II, K. Ashley, and J. Richer, *J. Electroanal. Chem.* **364**, 281 (1994).
  - [48] Z. Shi and J. Lipkowski, *J. Electroanal. Chem.* **364**, 289 (1994).
  - [49] Z. Shi and J. Lipkowski, *J. Electroanal. Chem.* **365**, 303 (1994).
  - [50] Z. Shi, S. Wu, and J. Lipkowski, *Electrochim. Acta* **40**, 9 (1995).
  - [51] Z. Shi, J. Lipkowski, S. Mirwald, and B. Pettinger, *J. Electroanal. Chem.* in press (1995).
  - [52] O. M. Magnussen, J. Hotlos, R. J. Nichols, D. M. Kolb, and R. J. Behm, *Phys. Rev. Lett.* **64**, 2929 (1990).
  - [53] D. M. Kolb, *Ber. Bunsenges. Phys. Chem.* **98**, 1421 (1994).
  - [54] S. Manne, P. K. Hansma, J. Massie, V. B. Elings, and A. A. Gewirth, *Science* **251**, 183 (1991).
  - [55] D. B. Parry, M. G. Samant, H. Seki, and M. R. Philpott, *Langmuir* **9**, 1878 (1993).
  - [56] L. Blum, H. D. Abruña, J. White, J. G. Gordon, II, G. L. Borges, M. G. Samant, and

- O. R. Melroy, J. Chem. Phys. **85**, 6732 (1986).
- [57] O. R. Melroy, M. G. Samant, G. L. Borges, J. G. Gordon, II, L. Blum, J. White, M. J. Albarelli, M. McMillan, and H. D. Abruña, Langmuir **4**, 728 (1988).
- [58] A. Tadjeddine, D. Guay, M. Ladouceur, and G. Tourillon, Phys. Rev. Lett. **66**, 2235 (1991).
- [59] J. G. Gordon, O. R. Melroy, and M. F. Toney, Electrochim. Acta **40**, 3 (1994).
- [60] M. F. Toney, J. N. Howard, J. Richer, G. L. Borges, J. G. Gordon, II, O. R. Melroy, D. Yee, and L. B. Sorenson, submitted to Phys. Rev. Lett.
- [61] Y. Nakai, M. S. Zei, D. M. Kolb, and G. Lempfuhr, Ber. Bunsenges. Phys. Chem. **88**, 340 (1984).
- [62] D. M. Kolb, K. Al Jaaf-Golze, and M. S. Zei, *Dechema-Monographien Band 102* (VCH Verlagsgesellschaft, Weinheim, 1986), p. 53.
- [63] D. M. Kolb, Z. Phys. Chem. Neue Folge **154**, 179 (1987).
- [64] Z. Shi, J. Lipkowski, M. Gamboa, P. Zelenay, and A. Wieckowski, J. Electroanal. Chem. **366**, 317 (1994).
- [65] O. M. Magnussen, J. Hageböck, J. Hotlos, and R. J. Behm, Faraday Discuss. **94**, 329 (1992).
- [66] G. J. Edens, X. Gao, and M. J. Weaver, J. Electroanal. Chem. **375**, 357 (1994).
- [67] P. Mrozek, M. Han, Y.-E. Sung, and A. Wieckowski, Surf. Sci. **319**, 21 (1994).
- [68] Y. Shingaya, H. Matsumoto, H. Ogasawara, and M. Ito, Surf. Sci. **335**, 23 (1995).
- [69] M. H. Hölzle and D. M. Kolb, Ber. Bunsenges. Phys. Chem. **98**, 330 (1994).
- [70] M. H. Hölzle, U. Retter, and D. M. Kolb, J. Electroanal. Chem. **371**, 101 (1994).

- [71] M. Kamrath, D. Zurawski, and A. Wieckowski, *Langmuir* **6**, 1683 (1990).
- [72] Y.-E. Sung, S. Thomas, and A. Wieckowski, *J. Phys. Chem*, in press.
- [73] P. Thiel and T. Madey, *Surf. Sci. Rep.* **7**, 211 (1988).
- [74] P. Mrozek, Y.-E. Sung, and A. Wieckowski, *Surf. Sci.* **335**, 44 (1995).
- [75] C. Pascard-Billy, *Acta Cryst.* **18**, 829 (1965).
- [76] See, *e.g.*, Table 1.4 of C. Kittel, *Introduction to Solid State Physics, Sixth Ed.* (Wiley, New York, 1986).
- [77] T. L. Einstein, *Surf. Sci.* **84**, L497 (1979).
- [78] S. H. Payne, J. Zhang, and H. J. Kreuzer, *Surf. Sci.* **264**, 185 (1992).
- [79] D. A. Huckaby and L. Blum, *J. Chem. Phys.* **97**, 5773 (1992).
- [80] R. J. Baxter, *Exactly Solved Models in Statistical Mechanics* (Academic, London, 1982).
- [81] A. J. Bard and L. R. Faulkner, *Electrochemical Methods: Fundamentals and Applications* (Wiley, New York, 1980).
- [82] A recent review of the kinetics of first-order phase transitions in lattice-gas models can be found in: P. A. Rikvold and B. M. Gorman, in *Annual Reviews of Computational Physics I*, edited by D. Stauffer (World Scientific, Singapore, 1994), p. 149.
- [83] G. M. Buendia, M. A. Novotny, and J. Zhang, in *Computer Simulation Studies in Condensed Matter Physics VII*, edited by D. P. Landau, K. K. Mon, and H. B. Schüttler (Springer, Berlin, 1994).
- [84] D. P. Landau, *Phys. Rev. B* **27**, 5604 (1983).
- [85] H. Kitatani and T. Oguchi, *J. Phys. Soc. Jpn.* **57**, 1344 (1988).
- [86] S. de Queiroz and E. Domany, preprint cond-mat/9507076.

- [87] F. Hommeril and B. Mutaftschiev, Phys. Rev. B **40**, 296 (1989).
- [88] D. Armand and M. L. Rosinberg, J. Electroanal. Chem. **302**, 191 (1991).
- [89] A comparison of results of perturbative and nonperturbative calculations for one and the same two-dimensional lattice-gas model is given by: P. A. Rikvold and M. A. Novotny, in *Condensed Matter Theories, Vol. 8*, edited by L. Blum and F. B. Malik (Plenum, New York, 1993), p. 627.
- [90] V. Pereyra, P. Nielaba, and K. Binder, J. Phys.: Cond. Matt. **5**, 6631 (1993).
- [91] T. Asselmeyer and W. Ebeling, submitted to Phys. Rev. E.
- [92] M. Blume, Phys. Rev. **141**, 517 (1966); H. W. Capel, Physica **32**, 966 (1966); M. Blume, V. J. Emery, and R. B. Griffiths, Phys. Rev. A **4**, 1071 (1971).
- [93] J. B. Collins, P. A. Rikvold, and E. T. Gawlinski, Phys. Rev. B **38**, 6741 (1988).
- [94] J. D. Kimel, P. A. Rikvold, and Y.-L. Wang, Phys. Rev. B **45**, 7237 (1992).
- [95] R. J. Baxter and P. A. Pearce, J. Phys. A **15**, 897 (1982); A. Klümper and P. A. Pearce, J. Stat. Phys. **64**, 13 (1991).
- [96] P. A. Rikvold, Phys. Rev. B **32**, 4756 (1985); **33**, 6523E (1986).
- [97] P. J. Feibelman, Ann. Rev. Phys. Chem. **40**, 261 (1989).
- [98] T. L. Einstein, in *Physical Structure of Solid Surfaces*, edited by W. N. Unertl, Handbook of Surface Science (Elsevier North-Holland, Amsterdam, 1995), Vol. 2.

## TABLES

TABLE I. Representative experimental conditions employed in the present paper and in some other voltammetric studies. The peak separations are calculated as averages over positive- and negative-going potential scans and are taken from figures or tables in the cited references.

Reference	Electrolyte	Peak separation	Scan rate
This work	1 mM CuSO <sub>4</sub> + 0.1 mM H <sub>2</sub> SO <sub>4</sub>	100 mV	2 mV/s
Kolb <i>et al.</i> [62,63]	1 mM CuSO <sub>4</sub> + 50 mM H <sub>2</sub> SO <sub>4</sub>	160 mV	1 mV/s
Schultze <i>et al.</i> [7]	1 M HClO <sub>4</sub> + 1 mM Cu <sup>2+</sup> + 1 mM SO <sub>4</sub> <sup>2-</sup>	130 mV	20 mV/s
Shi <i>et al.</i> [48,49]	1 mM Cu(ClO <sub>4</sub> ) <sub>2</sub> + 5 mM K <sub>2</sub> SO <sub>4</sub> + 0.1 M HClO <sub>4</sub>	140 mV	5 mV/s
Omar <i>et al.</i> [46]	5 mM CuSO <sub>4</sub> + 90 mM H <sub>2</sub> SO <sub>4</sub>	150 mV	5 mV/s

TABLE II. List of ordered phases  $(X \times Y)_{\Theta_C}^{\Theta_S}$  and their ground-state energies per site. Only those phases are included that are realized as ground states for interactions in the region of experimental interest.

	Phase	Ground-state energy per site
1	$(1 \times 1)_0^0$	0
2	$(1 \times 1)_1^0$	$-\bar{\mu}_C - 3\Phi_{CC}^{(1)} - 3\Phi_{CC}^{(2)}$
3	$(\sqrt{3} \times \sqrt{3})_{2/3}^{1/3}$	$-(\bar{\mu}_S + 2\bar{\mu}_C)/3 - \Phi_{CC}^{(1)} - 2\Phi_{CC}^{(2)} - 2\Phi_{SC}^{(1)} - \Phi_{SS}^{(2)} - 2\Phi_{SS}^{(t)}/3$
4	$(\sqrt{3} \times \sqrt{3})_{1/3}^{1/3}$	$-(\bar{\mu}_S + \bar{\mu}_C)/3 - \Phi_{CC}^{(2)} - \Phi_{SC}^{(1)} - \Phi_{SS}^{(2)} - 2\Phi_{SS}^{(t)}/3$
5	$(\sqrt{3} \times \sqrt{3})_{2/3}^0$	$-2\bar{\mu}_C/3 - \Phi_{CC}^{(1)} - 2\Phi_{CC}^{(2)}$
6	$(\sqrt{3} \times \sqrt{3})_0^{1/3}$	$-\bar{\mu}_S/3 - \Phi_{SS}^{(2)} - 2\Phi_{SS}^{(t)}/3$
7	$(\sqrt{3} \times \sqrt{3})_{1/3}^0$	$-\bar{\mu}_C/3 - \Phi_{CC}^{(2)}$
8	$(\sqrt{3} \times \sqrt{7})_{4/5}^{1/5}$	$-(\bar{\mu}_S + 4\bar{\mu}_C + \Phi_{SS}^{(2)} + 2\Phi_{SS}^{(4)} + 9\Phi_{CC}^{(1)} + 10\Phi_{CC}^{(2)} + 6\Phi_{SC}^{(1)})/5$
9	$(\sqrt{7} \times \sqrt{7})_0^{1/7}$	$-(\bar{\mu}_S + 3\Phi_{SS}^{(4)})/7$
10	$(\sqrt{3} \times \sqrt{7})_0^{1/5}$	$-(\bar{\mu}_S + \Phi_{SS}^{(2)} + 2\Phi_{SS}^{(4)})/5$



TABLE III. CV peak positions and separations for different electrolyte compositions at a potential scan rate of 10 mV/s, from Ref. [46]. The compositions used were  $x$  mM CuSO<sub>4</sub> + 90 mM H<sub>2</sub>SO<sub>4</sub>. The peak positions given in the table are in mV *vs.* the Normal Hydrogen Electrode. They are averages over the positive- and negative-going scans in Fig. 4 of Ref. [46], taken from Table 2 of Ref. [23]. These results are used in calculating the effective electrovalences in Subsec. IV C.

$x$	Peak #1	Peak #2	Peak separation
0.5	444 mV	303 mV	141 mV
5.0	496 mV	327 mV	169 mV
50	554 mV	352 mV	202 mV

## FIGURES

FIG. 1. (a) Our experimental CV current densities for a Au(111) electrode in 0.1 mM  $\text{H}_2\text{SO}_4$  at a potential scan rate of 10 mV/s (dotted curve) and in 1 mM  $\text{CuSO}_4$  + 0.1 mM  $\text{H}_2\text{SO}_4$  at 2 mV/s (solid and dash-dotted curves). The differences between the latter two curves provide a measure of the experimental uncertainties. The arrows indicate the potential-scan directions. Note that the current density is proportional to the scan rate. Thus, the copper-free voltammogram corresponds to a very small charge transfer per unit potential change, compared to the copper-containing case. (b) Integrated charge density for the positive-going scan with  $\text{Cu}^{2+}$ -containing electrolyte (solid curve). [The corresponding current density is the dash-dotted curve in panel (a), which for clarity is also shown against the right-hand vertical axis in this panel.] The charge density is defined as zero at +366 mV *vs.* Ag/AgCl.

FIG. 2. Auger electron spectra at 3 keV of the Au(111) electrode covered by underpotentially deposited Cu and coadsorbed sulfate. The emersions were carried out at several electrode potentials, as indicated *vs.* Ag/AgCl. These data were used to calculate the Cu and sulfate coverages shown in Figs. 7 and 8.

FIG. 3. The  $(\sqrt{3} \times \sqrt{3})\text{R}30^\circ$  LEED pattern at 91.1 eV electron energy, obtained from the Au(111) electrode emersed from the 1 mM  $\text{CuSO}_4$  + 0.1 mM  $\text{H}_2\text{SO}_4$  solution at  $E=220$  mV *vs.* Ag/AgCl, which is in the potential region between the two CV peaks shown in Fig. 1.

FIG. 4. The relative positions of Cu ( $\bullet$ ) and sulfate ( $\triangle$ ) corresponding to the effective interactions in Eq. (1). The number underneath each bond representation is the corresponding effective interaction energy obtained in this work, given in kJ/mol. In particular, the configuration corresponding to  $\Phi_{\text{SS}}^{(1)}$ , in which the corners of the sulfate triangles touch, is forbidden; hence the infinitely strong “hard-hexagon” repulsion. The interactions are invariant under symmetry operations on the lattice.

FIG. 5. The ground-state diagram obtained with the effective interaction constants given in Fig. 4. The zero-temperature phase boundaries are represented by the solid lines, and the phases are indicated as  $(X \times Y)_{\Theta_C}^{\Theta_S}$ . Superimposed on the ground-state diagram are the positions of CV Peak #1 (filled diamonds) and Peak #2 (filled squares) at room temperature. The three points marked  $\bullet$  are low maxima associated with Cu adsorption without coadsorbed sulfate. The potential scan path for the simulation corresponding to our experiments with the 1 mM  $\text{CuSO}_4$  + 0.1 mM  $\text{H}_2\text{SO}_4$  electrolyte is shown as the dotted line labeled “1,” whereas the lines labeled “2” and “3” correspond to additional simulations for 5 mM and 0.2 mM  $\text{Cu}^{2+}$  with unchanged sulfate concentration, respectively. For all three lines, the upper, left end point corresponds to 120 mV *vs.* Ag/AgCl, and the lower, right end point corresponds to 420 mV.

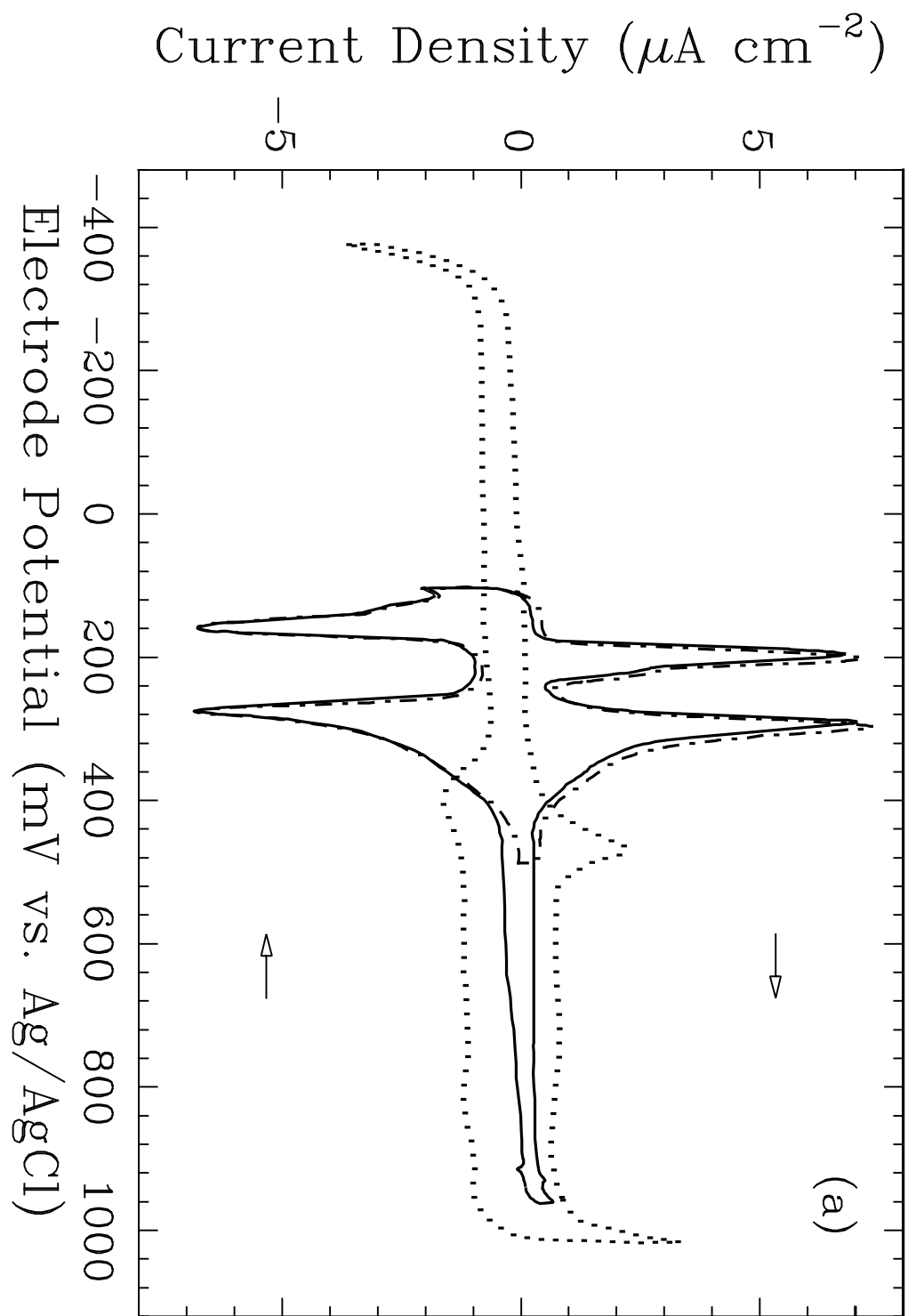
FIG. 6. (a) Experimental (dot-dashed) and simulated (solid) CV current densities. The experimental curve is the same as the positive-going scan shown in Fig. 1(b). The left-hand vertical scale shows the current density for a scan rate of 2 mV/s, whereas the right-hand scale shows the current density normalized by the scan rate, in units of elementary charges per mV and Au(111) unit cell. (b) Experimental (dot-dashed) and simulated (solid) integrated charge transfers. The experimental curve is the same as shown in Fig. 1(b). The dashed and long-dashed curves represent the simulated, partial charge density corresponding to copper and sulfate, respectively. The experimental charge density is defined as zero at +366 mV. The data points marked  $\times$  in both panel (a) and (b) represent additional simulation results for  $L=45$ . They show that finite-size effects in the simulations are negligible, except very close to the maxima of the CV peaks.

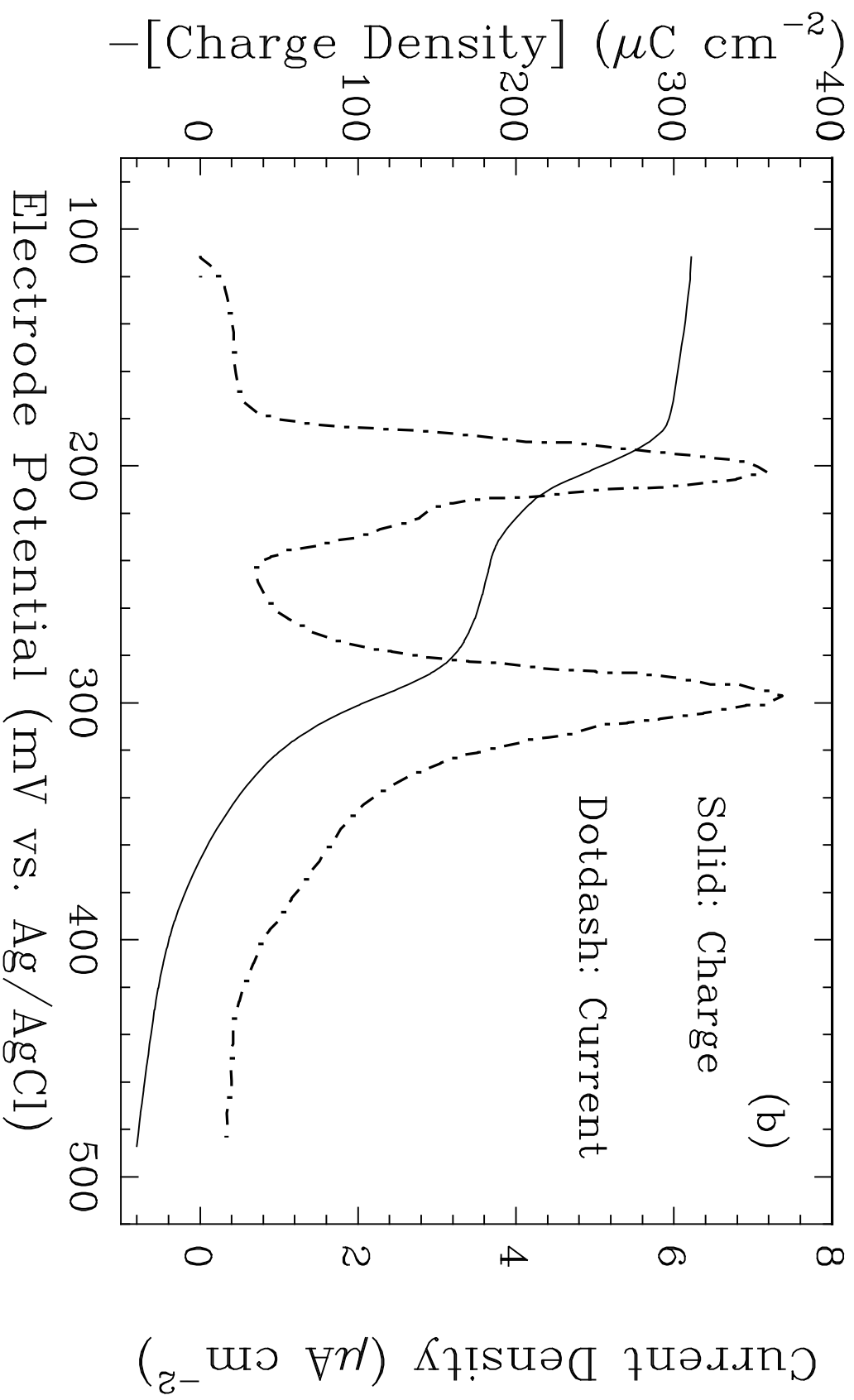
FIG. 7. Simulated coverages of Cu,  $\Theta_C$  (dashed), first-layer sulfate,  $\Theta_S$  (dotted), and total sulfate,  $\Theta_S + \Theta_S^{(2)}$  (long-dashed), shown together with the corresponding results from our AES experiments,  $\square$  and  $\diamond$ , respectively.

FIG. 8. (a) The total sulfate coverage,  $\Theta_S + \Theta_S^{(2)}$ , shown *vs.*  $\Theta_C$ . The data points shown as crossed error bars represent the AES data from Fig. 7. (b) Finite-difference estimate of the differential coadsorption ratio  $d(\Theta_S + \Theta_S^{(2)})/d\Theta_C$  as a function of  $\Theta_C$ . The ratio exhibits a broad maximum, corresponding to the linear section in panel (a), indicative of mutually enhanced adsorption.

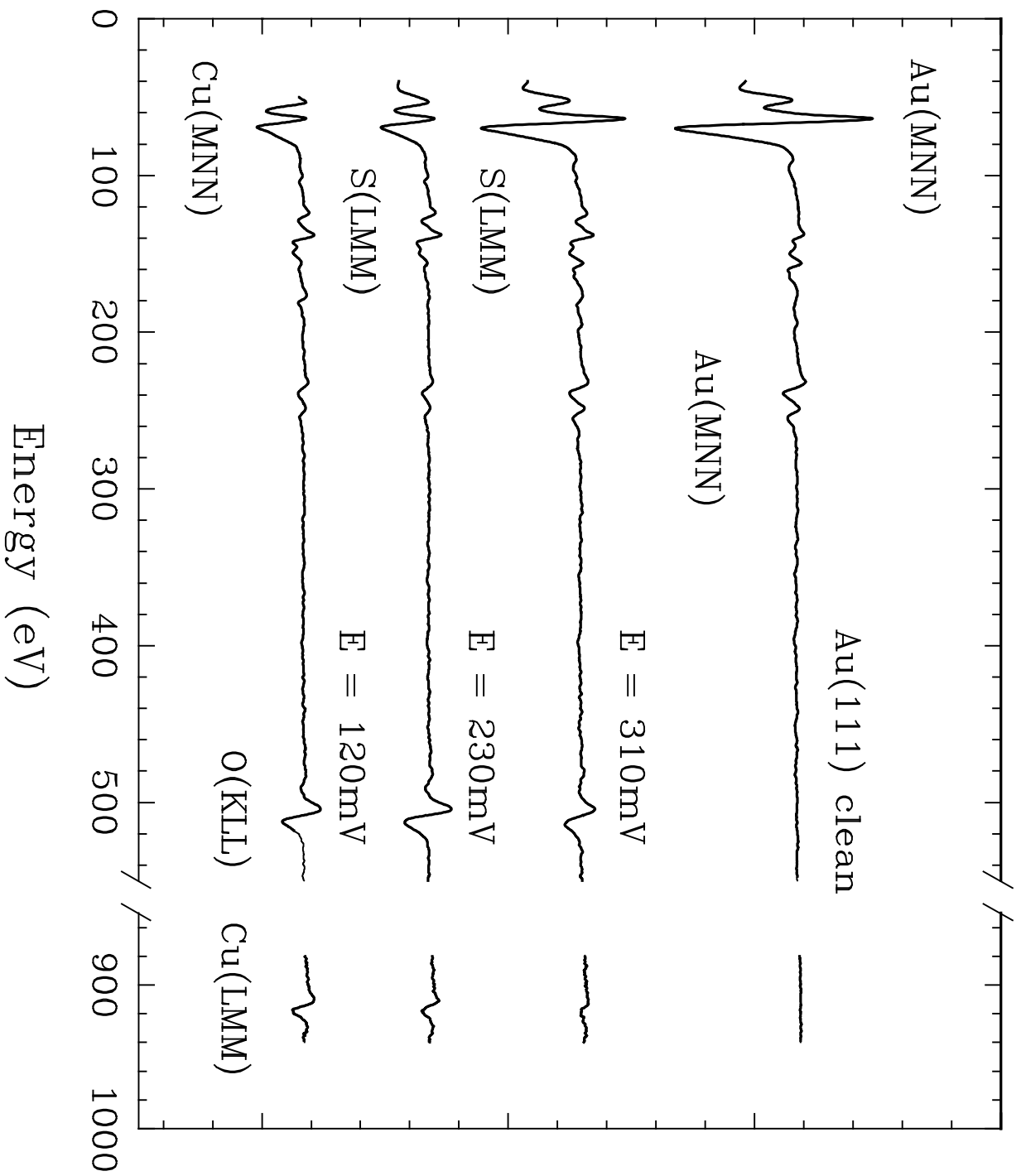
FIG. 9. Simulation results for Path 2 (5 mM  $\text{Cu}^{2+}$ ) and Path 3 (0.2 mM  $\text{Cu}^{2+}$ ) in Fig. 5. (a) CV current densities for Path 2 (dashed) and Path 3 (solid). (b) Coverages for Path 2 ( $\Theta_C$ : dashed;  $\Theta_S + \Theta_S^{(2)}$ : dot-dashed) and Path 3 ( $\Theta_C$ : solid;  $\Theta_S + \Theta_S^{(2)}$ : dotted).

FIG. 10. Finite-size scaling plots of the maximum values of the dimensionless adsorbate heat capacity,  $C/R$ , and nonordering response functions,  $-RT(\partial Q/\partial D)$  and  $RT(\partial M/\partial H)$ , for system sizes  $L=15, 30$ , and  $45$ . The straight lines are unweighted least-squares fits to the data points. See details in Sec. VI. (a) At Peak #1, showing  $C/R$  ( $\diamond$  and solid line) and  $-RT(\partial Q/\partial D)$  ( $\square$  and dashed line) *vs.*  $L^2$ . The response function has been divided by 10 for easy visual comparison with the heat capacity. (b) At Peak #2, showing  $C/R$  ( $\diamond$  and solid line) and  $RT(\partial M/\partial H)$  ( $\circ$  and dot-dashed line) *vs.*  $L^{2/5}$ .



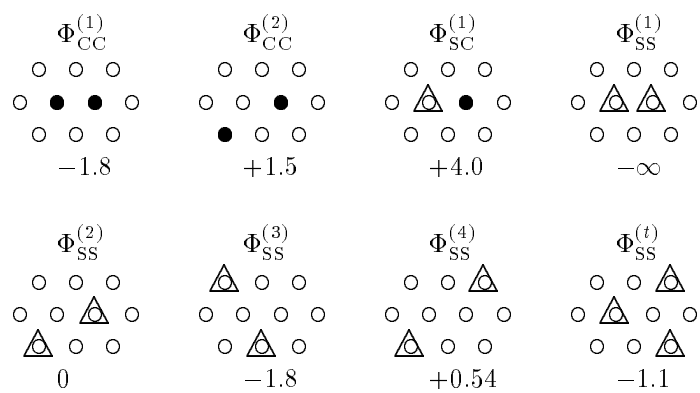


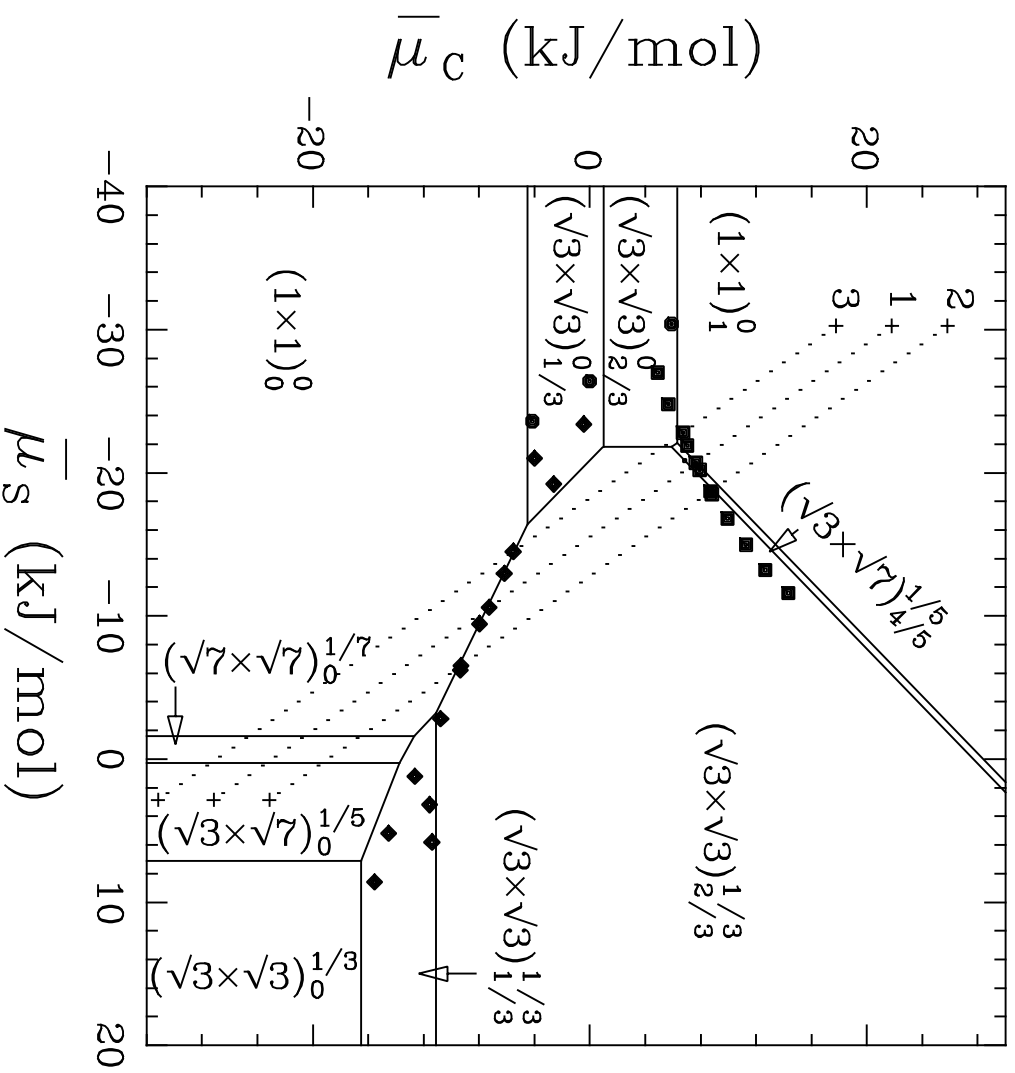
$E dN(E)/dE$  (arbitrary units)

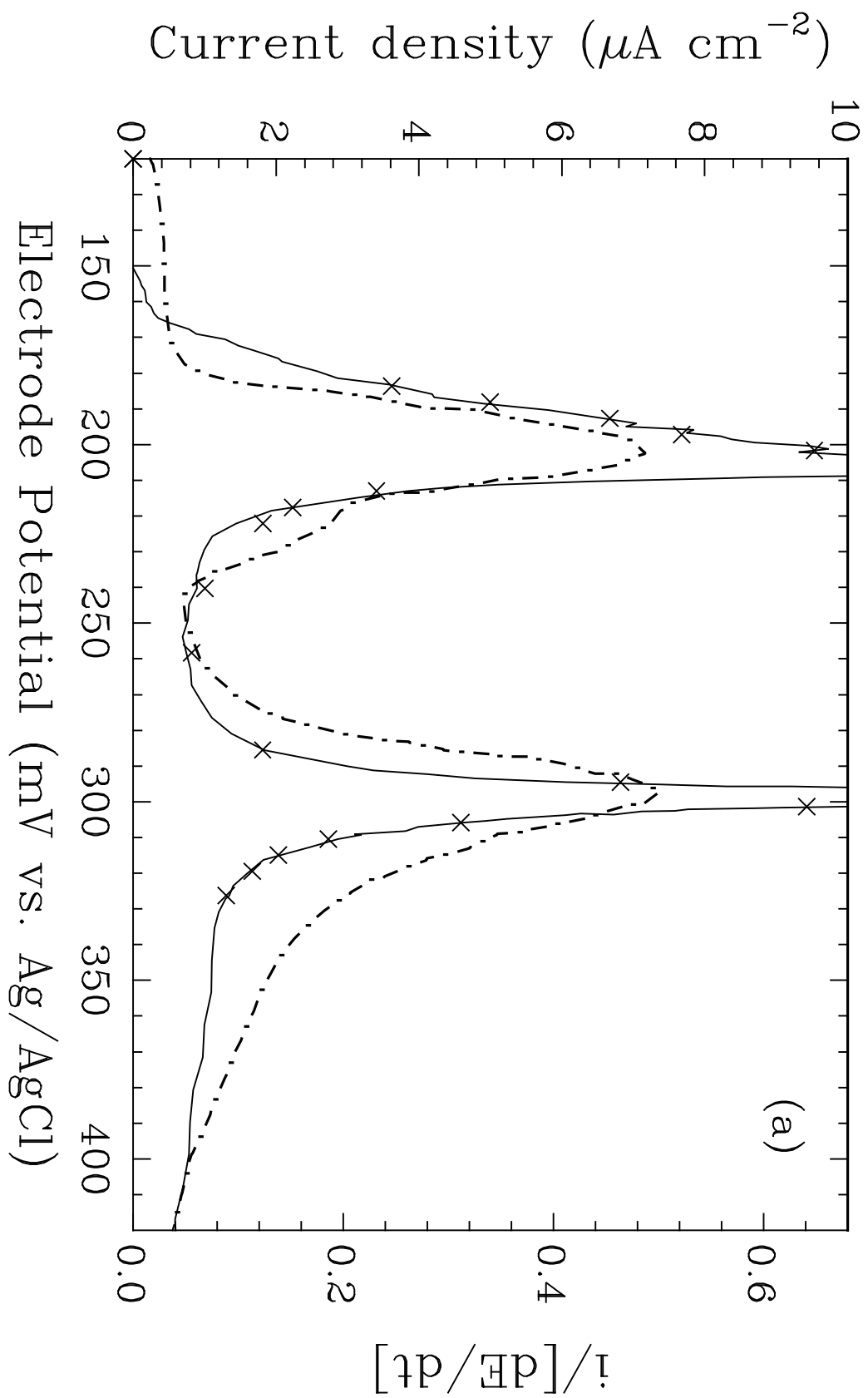


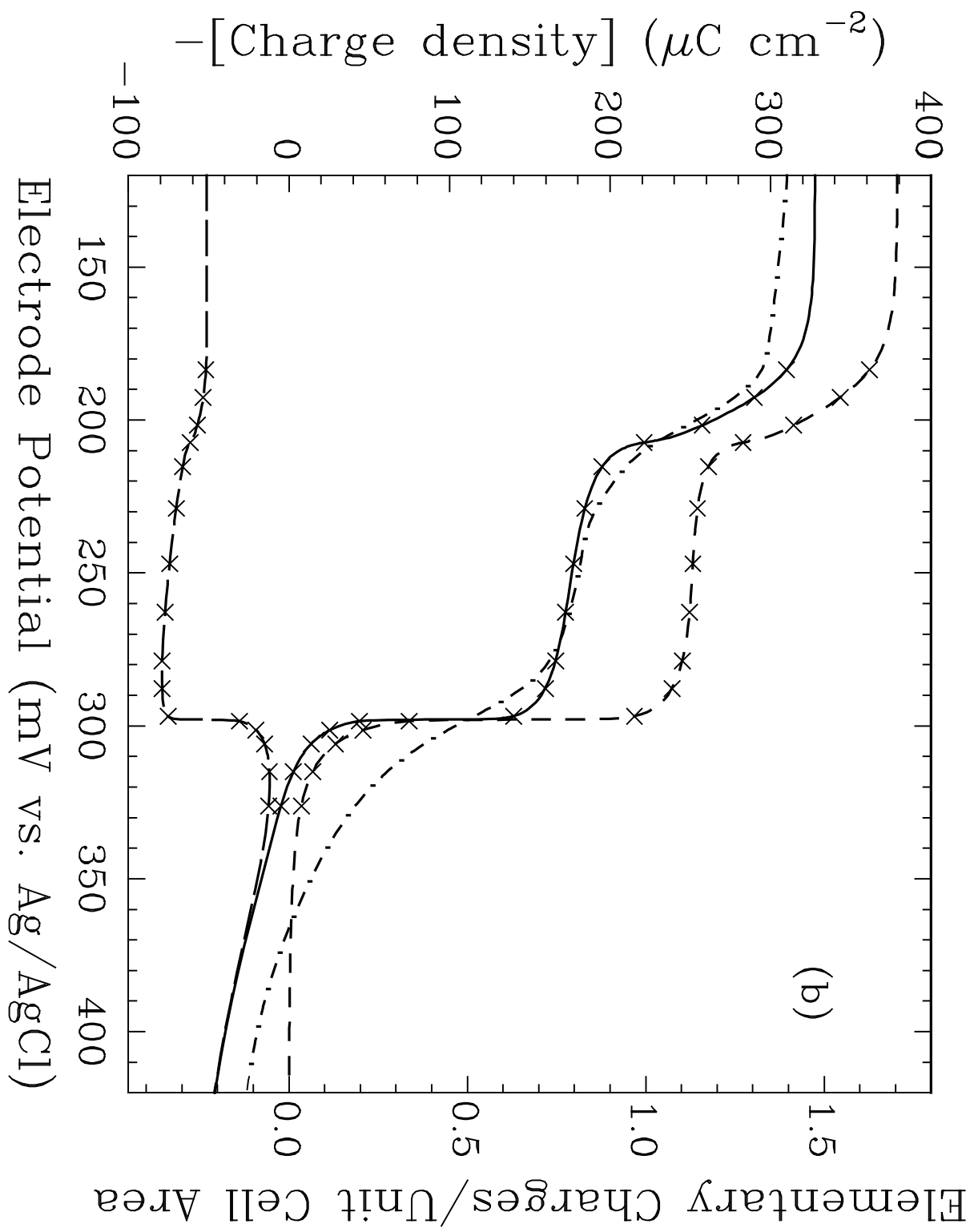


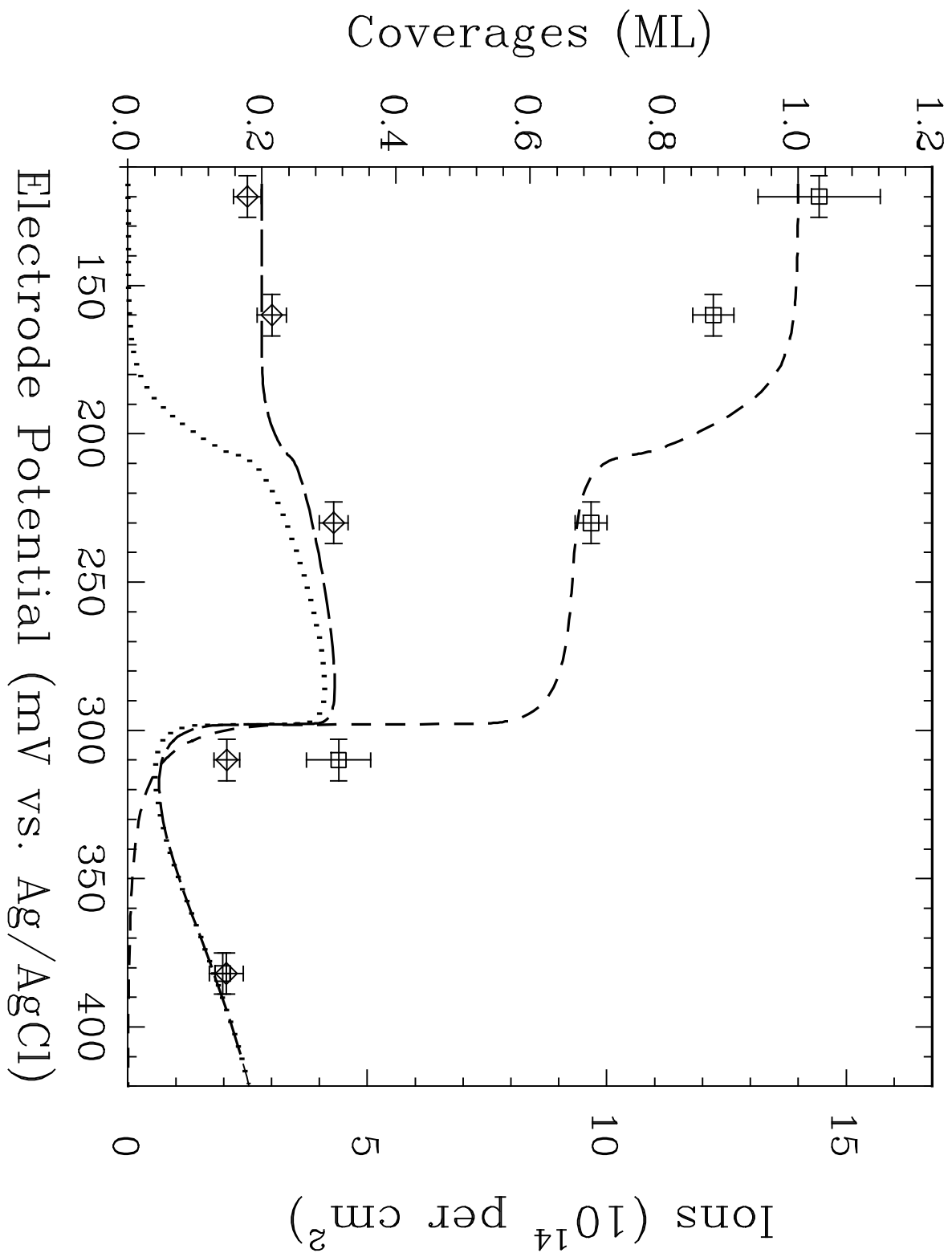


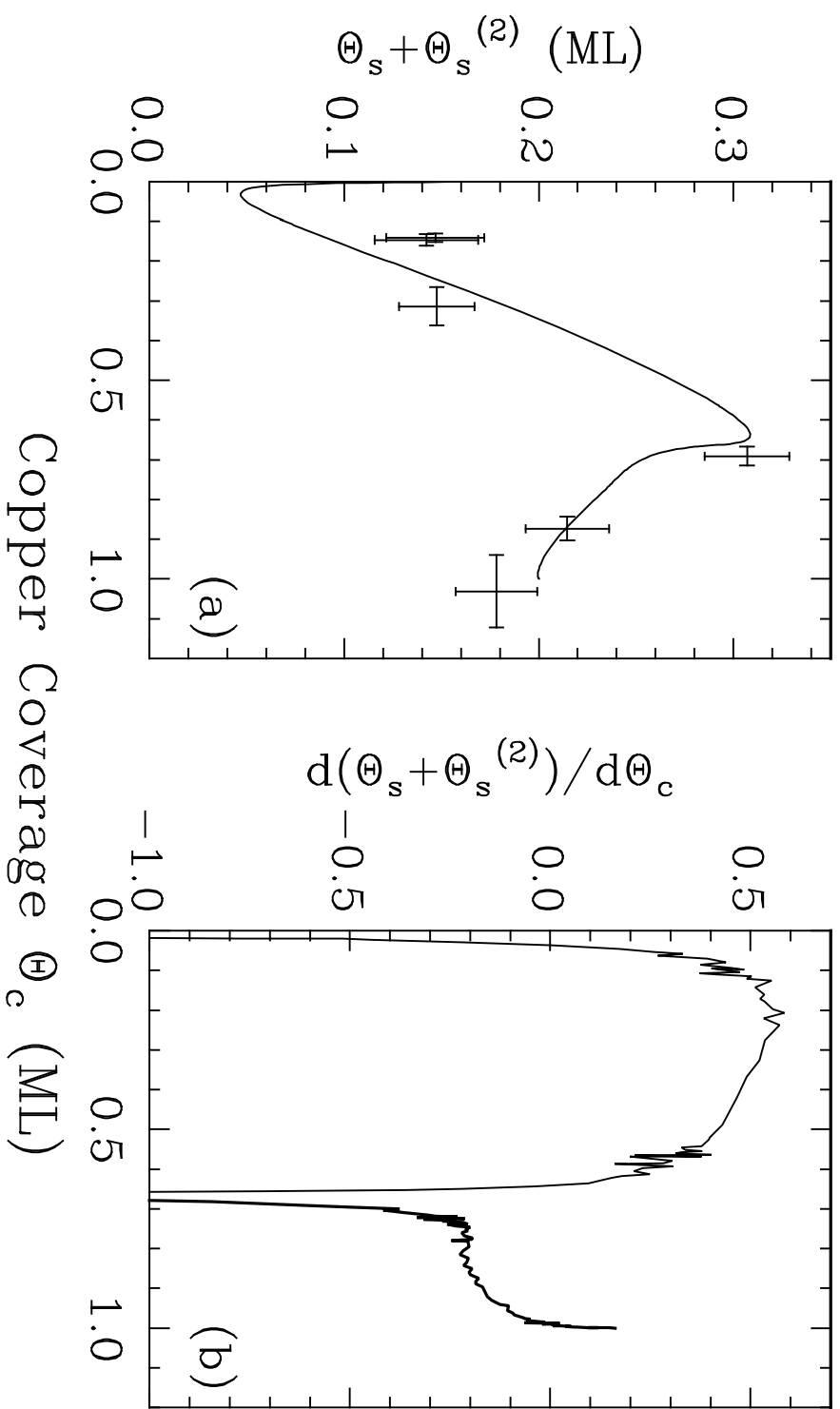


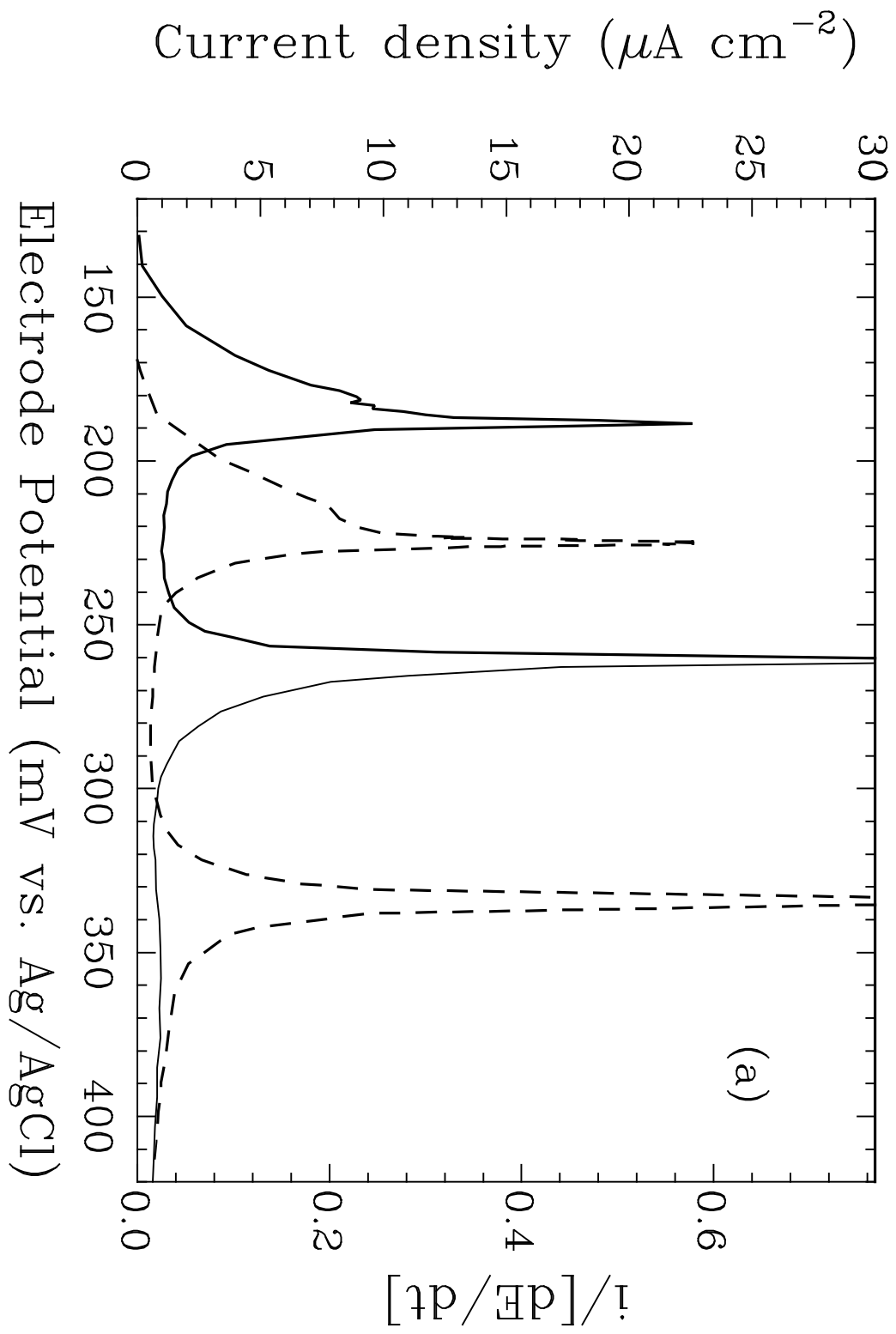


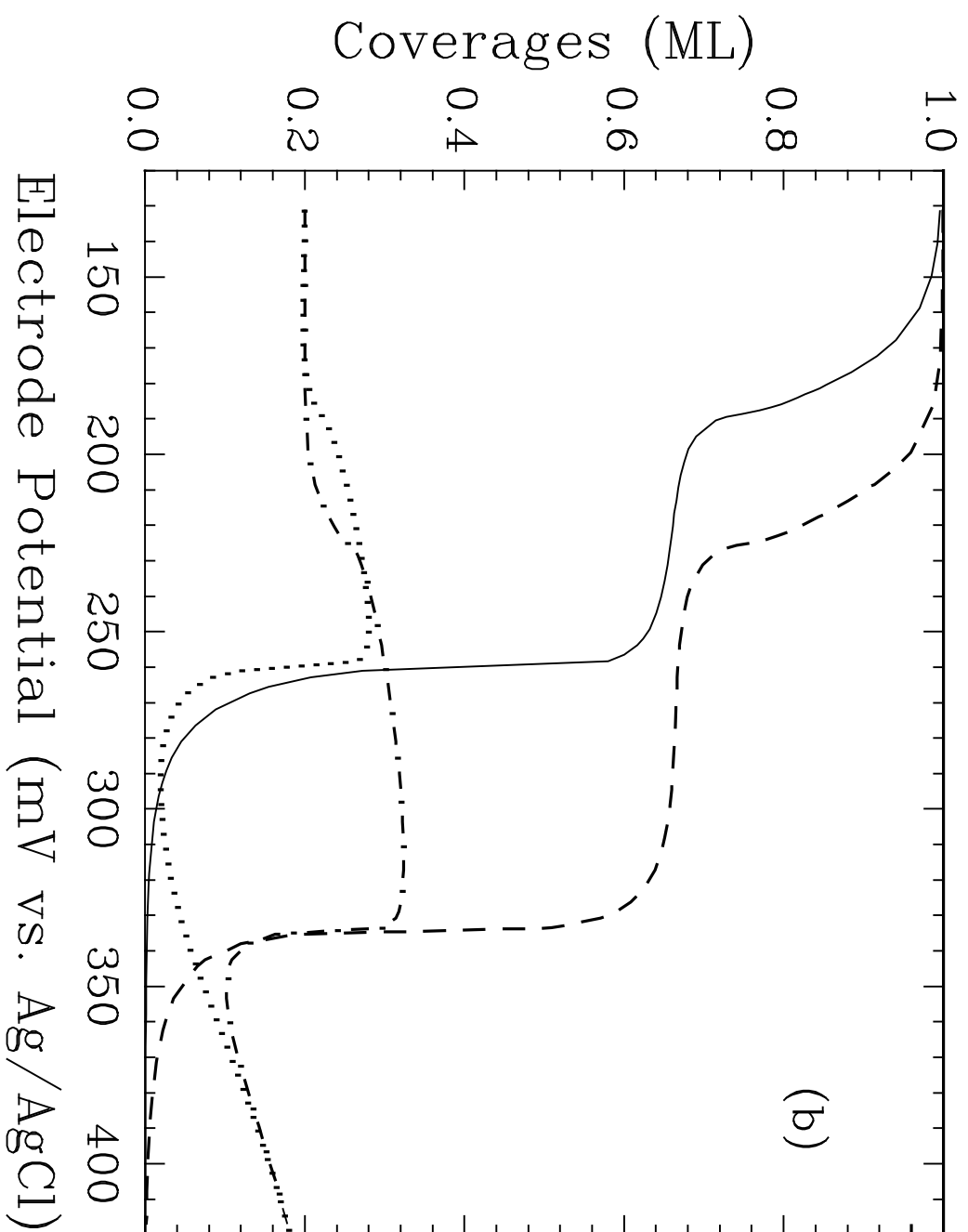






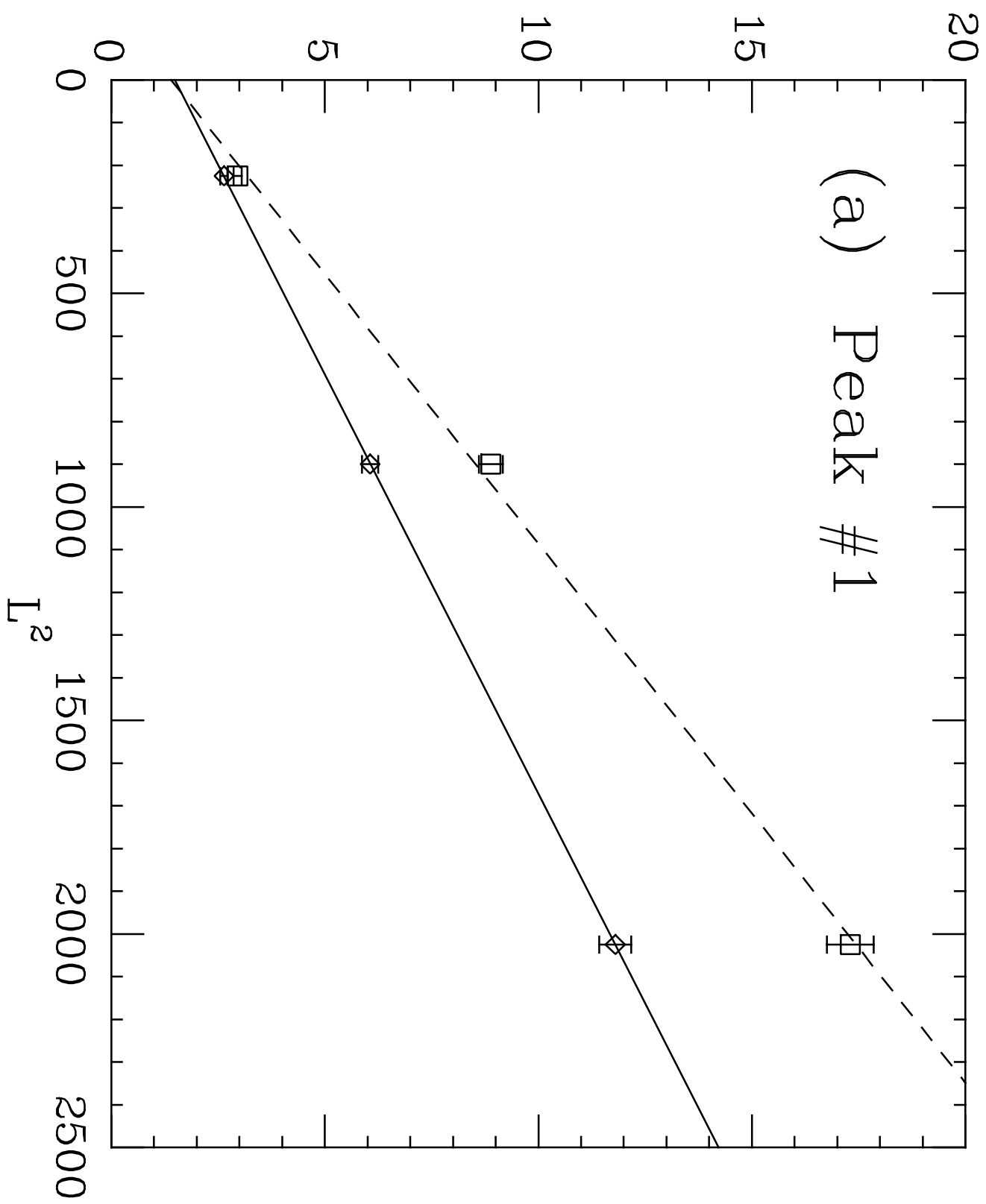








$$C/R, \quad -RT(\partial Q/\partial D)/10$$



C/R,  $RT(\partial M/\partial H)$

(b) Peak #2

